

Article

Biom mineralization of Monohydrocalcite Induced by the Halophile *Halomonas Smyrnensis* WMS-3

Juntong Pan ^{1,2,†}, Hui Zhao ^{1,2,†} , Maurice E. Tucker ^{3,4}, Jingxuan Zhou ¹, Mengzhen Jiang ¹, Yapeng Wang ¹, Yanyang Zhao ¹, Bin Sun ¹, Zuozhen Han ^{1,2,*} and Huaxiao Yan ^{1,*}

¹ College of Chemical and Environmental Engineering, College of Earth Science and Engineering, Shandong Provincial Key Laboratory of Depositional Mineralization and Sedimentary Minerals, Shandong University of Science and Technology, Qingdao 266590, China; panjuntong1125@163.com (J.P.); zhsdust@126.com (H.Z.); 15689435926@163.com (J.Z.); jj17865085532@163.com (M.J.); wyp1932176949@163.com (Y.W.); 18765927620@163.com (Y.Z.); sunbin2012@163.com (B.S.)

² Laboratory for Marine Mineral Resources, Center for Isotope Geochemistry and Geochronology, Qingdao National Laboratory for Marine Science and Technology, Qingdao 266237, China

³ School of Earth Sciences, University of Bristol, Bristol BS8 1RJ, UK; glmet@bristol.ac.uk

⁴ Cabot Institute, University of Bristol, Cantock's Close, Bristol BS8 1UJ, UK

* Correspondence: hanzuozhen65@126.com (Z.H.); 15954804511@163.com (H.Y.); Tel.: +86-532-86-057-055 (Z.H.); +86-532-86-057-625 (H.Y.)

† Hui Zhao and Juntong Pan contributed equally and as co-first authors.

Received: 1 September 2019; Accepted: 12 October 2019; Published: 15 October 2019



Abstract: The halophilic bacterium *Halomonas smyrnensis* from a modern salt lake used in experiments to induce biomineralization has resulted in the precipitation of monohydrocalcite and other carbonate minerals. In this study, a *Halomonas smyrnensis* WMS-3 (GenBank:MH425323) strain was identified based on 16S rDNA homology comparison, and then cultured in mediums with 3% NaCl concentration to induce monohydrocalcite at different Mg/Ca molar ratios of 0, 2, 5, 7, and 9. The growth curve of WMS-3 bacteria, pH values, NH_4^+ concentration, HCO_3^- and CO_3^{2-} concentration, carbonic anhydrase (CA) activity, and the changes in Ca^{2+} and Mg^{2+} ion concentration were determined to further explore the extracellular biomineralization mechanism. Moreover, the nucleation mechanism of monohydrocalcite on extracellular polymeric substances (EPS) was analyzed through studying ultrathin slices of the WMS-3 strain by High resolution transmission electron microscopy (HRTEM), Selected area electron diffraction (SAED), Scanning transmission electron microscopy (STEM), and elemental mapping, besides this, amino acids in the EPS were also analyzed. The results show that pH increased to about 9.0 under the influence of ammonia and CA activity. The precipitation ratio (% the ratio of the mass/volume concentration) of the Ca^{2+} ion was 64.32%, 62.20%, 60.22%, 59.57%, and 54.42% at Mg/Ca molar ratios of 0, 2, 5, 7, and 9, respectively, on the 21st day of the experiments, and 6.69%, 7.10%, 7.74%, 8.09% for the Mg^{2+} ion concentration at Mg/Ca molar ratios 2, 5, 7, and 9, respectively. The obtained minerals were calcite, Mg-rich calcite, aragonite, and hydromagnesite, in addition to the monohydrocalcite, as identified by X-ray diffraction (XRD) analyses. Monohydrocalcite had higher crystallinity when the Mg/Ca ratio increased from 7 to 9; thus, the stability of monohydrocalcite increased, also proven by the thermogravimetry (TG), derivative thermogravimetry (DTG) and differential scanning calorimetry (DSC) analyses. The C=O and C–O–C organic functional groups present in/on the minerals analyzed by Fourier transform infrared spectroscopy (FTIR), the various morphologies and the existence of P and S determined by scanning electron microscope-energy dispersive spectrometer (SEM-EDS), the relatively more negative stable carbon isotope values (−16.91‰ to −17.91‰) analyzed by a carbon isotope laser spectrometer, plus the typical surface chemistry by XPS, all support the biogenesis of these mineral precipitates. Moreover, Ca^{2+} ions were able to enter the bacterial cell to induce intracellular biomineralization. This study is useful to understand the mechanism of biomineralization further and may provide theoretical reference concerning the formation of monohydrocalcite in nature.

Keywords: *Halomonas smyrnensis*; biomineralization; monohydrocalcite; nucleation site; Mg/Ca ratios

1. Introduction

Calcium carbonate is of great scientific significance in biomineralization and the Earth Sciences generally. The formation of calcium carbonate through microbial activities, as well as plankton, acting on a global scale and utilizing huge quantities of CO₂, can affect the chemistry of ocean water, the Earth's atmosphere, and climate [1–5]. Although there is ample evidence that 3.5 Ga stromatolites are biogenic [6,7], the potential role of abiotic processes in the formation of these laminated structures remains controversial [8]. Regardless of stromatolites formed in the past, contemporary microbial mats provide insight into the important role played by microbes in the precipitation of minerals. Understanding microbially-mediated precipitation of carbonate minerals is critical for the interpretation of the rock record and is also one of the fundamental research objectives in the rapidly expanding field of biogeosciences [9–14].

Calcium carbonate minerals at Earth's surface conditions include the common polymorphs calcite, aragonite, and vaterite, and the less common hydrated phases of monohydrocalcite (CaCO₃·H₂O) and ikaite (CaCO₃·6H₂O) [15–27]. It has been reported that monohydrocalcite is metastable compared with calcite and aragonite at all temperatures and pressures [28]. Maybe due to this reason, monohydrocalcite is not widely distributed in the world. Previously, monohydrocalcite has only been found in fresh-water and terrestrial environments. Dahl and Buchardt (2006) reported that monohydrocalcite is a common mineral (up to 55%) in the debris fragments of ikaite (CaCO₃·6H₂O) tufa columns formed in the cold marine Ikka fjord, SW Greenland [28]. In fact, before monohydrocalcite was discovered in the marine environment, it had been induced by the moderately halophilic species *Halomonas eurihalina* and *Bacillus siamensis* in both solid and liquid media in the laboratory; at that time, the focus was on the influence of salinity and temperature on the minerals precipitated [29–31]. Later, *Halobacillus trueperi* bacteria were also used to induce monohydrocalcite in both solid and liquid media at different salt concentrations and different Mg/Ca ratios [32]. *Rhodococcus erythropolis* [33], *Chromohalobacter israelensis* [34] and *Chromohalobacter marismortui* [35] were also used to induce the formation of monohydrocalcite in the laboratory. However, there are fewer studies on the mechanism of monohydrocalcite biomineralization, the nucleation sites, the nucleation mechanism, and intracellular biomineralization. Moreover, using *H. smyrnensis* bacteria to induce the biomineralization of monohydrocalcite has also been rarely reported.

In this study, the *H. smyrnensis* WMS-3 strain was identified based on 16S rDNA sequence homology analysis, and then used to induce carbonate minerals at different Mg/Ca molar ratios 0, 2, 5, 7, and 9 at a 3% NaCl concentration that was similar to seawater salinity. The extracellular biomineralization mechanism was explored by analyzing the growth curve of WMS-3 bacteria, pH values, NH₄⁺ concentration, HCO₃⁻, and CO₃²⁻ concentration, carbonic anhydrase (CA) activity, and the changes in the concentration of Ca²⁺ and Mg²⁺ ions. The nucleation mechanism of minerals on extracellular polymeric substances (EPS) was analyzed through studying ultrathin slices of WMS-3 strain by high-resolution transmission electron microscopy (HRTEM), selected area electron diffraction (SAED), scanning transmission electron microscope (STEM), and elemental mapping; in addition, the amino acids in EPS were determined. At the same time, intracellular biomineralization was observed in ultrathin slices. The bacterially-induced minerals were investigated by X-ray powder diffraction (XRD), Fourier transform infrared spectroscopy (FTIR), scanning electron microscope coupled with energy dispersive spectroscopy (SEM-EDS), stable carbon isotope composition, and X-ray photoelectron spectroscopy (XPS). This study aims to understand the mechanism of biomineralization further and may provide insights into the formation of monohydrocalcite in nature.

2. Materials and Methods

2.1. Bacterial Strain and Culture Medium

The WMS-3 strain used in this study was isolated from the Yinjiashan saltern (Qingdao, China). WMS-3 bacteria were cultured in a liquid medium containing the following components (unit: $\text{g}\cdot\text{L}^{-1}$, pH 7.0): peptone 10, beef extract 5, NaCl 5, and distilled water 1 L. Twenty grams of agar powder were added into the above liquid culture medium to prepare the solid medium.

2.2. Identification of *H. smyrnensis* WMS-3 Bacteria

The preserved WMS-3 bacteria were sent to Shanghai Biological Engineering Co., Ltd. (Shanghai, China) for 16S rDNA sequencing, and the final 16S rDNA sequences were uploaded to the GenBank/NCBI database to obtain an accession number. The homology between the 16S rDNA sequences of WMS-3 and those of other bacteria in the GenBank/NCBI database was compared by Basic Local Alignment Search Tool (BLAST) analysis. The phylogenetic tree of WMS-3 was constructed by the neighbor-joining method in the MEGA 7 software (Version 7.0, The Pennsylvania State University, Philadelphia, PA, USA).

2.3. Characterization of *H. smyrnensis* WMS-3 Bacteria

2.3.1. Cell Morphology, Gram Staining, and Ammonia Test

The morphology of *H. smyrnensis* WMS-3 bacteria was analyzed by scanning electron microscope (SEM, S-4800, Hitachi, Tokyo, Japan). The detailed steps for performing the SEM and Gram staining experiments were according to the published reference by Han et al. [36]. The ammonia test was performed as reported by Zhuang et al. [37].

2.3.2. Bacterial Growth Curve and pH Changes

To determine the optimum salt concentration for the growth of *H. smyrnensis* WMS-3 bacteria, the culture mediums with 3%, 5%, 10%, 15%, 20%, 25%, and 30% NaCl concentration were prepared, respectively. The bacterial seed ($\text{OD}_{600} = 1.0$) was inoculated into the above mediums at an inoculation volume ratio of 1%, and then these cultures were cultivated in an oscillating incubator (HZQ-F160, Harbin Electronic Technology Development Co., Ltd., Harbin, China) with a speed of 120 rpm at 37 °C, after 24 h, the concentration of *H. smyrnensis* WMS-3 bacteria was measured by a spectrophotometer (722 s, Shanghai Analysis Instrument Factory, Shanghai, China) at a wavelength of 600 nm. From now on, WMS-3 bacteria were cultured in a medium with the optimum NaCl concentration to perform all the following experiments. The cell concentration was measured according to the above steps to draw the growth curve, and the pH values of the experimental and control groups were measured by a pH indicator (PHS-3C, Shanghai Shengke Instrument Equipment Co., Ltd., Shanghai, China). The difference between the experimental and control group was that the experimental group was inoculated with a bacterial seed ($\text{OD}_{600} = 1.0$) at an inoculation volume ratio of 1%, and the control group was inoculated with sterile distilled water at the same volume ratio of 1%. The difference in pH values between the experimental and control group was analyzed by the SPSS 21 software (Version 21.0, International Business Machines Corporation, Armonk, NY, USA).

2.3.3. NH_4^+ Concentrations and pH Values Based on NH_4^+ Concentrations

The concentration of NH_4^+ ions in the liquid culture medium inoculated with WMS-3 bacteria was measured using the method of Zhuang et al. [37]. Meanwhile, the pH values based on NH_4^+ concentrations were also calculated by the method of Zhuang et al. [37].

2.3.4. CA Activity, CO_3^{2-} and HCO_3^- Concentrations, and pH Values Based on CO_3^{2-} and HCO_3^- Concentrations

In this study, 1 unit of CA activity (U) was defined as the amount of enzyme required to release 1 μmol of p-nitrophenol per min and 1 L. The detailed steps for analyzing the CA activity and measuring the concentrations of CO_3^{2-} and HCO_3^- ions were all according to the methods of Zhuang et al. [37]. To further determine the role of CO_3^{2-} and HCO_3^- concentrations on pH changes ($\text{Na}_2\text{CO}_3 + \text{NaHCO}_3$) solutions were prepared based on the different CO_3^{2-} and HCO_3^- concentrations, and then the pH values of ($\text{Na}_2\text{CO}_3 + \text{NaHCO}_3$) solutions were measured.

2.4. Biomineralization Experiments

In the bacterially-induced biomineralization experiments, the components of the culture medium were the same as the above 2.1.; besides this, NaCl concentration was 3%, Ca^{2+} concentration was 0.01 M, and the Mg/Ca molar ratios were set to 0, 2, 5, 7, and 9 by using calcium chloride and magnesium chloride, respectively. The group inoculated with a bacterial seed ($\text{OD}_{600} = 1.0$) at an inoculation volume ratio 1% was set as the experimental group, and the other group inoculated with sterile distilled water at the same inoculation volume ratio for the control group. The pH values in these two groups were all adjusted to 7.0. All the cultures were incubated in a constant temperature shaker (HZQ-F160, Harbin Electronic Technology Development Co., Ltd., Harbin, China) with a speed of 115 rpm at 37 °C. The above experiments were performed in triplicate.

2.5. Concentrations of Ca^{2+} and Mg^{2+} Ions

The concentrations of Ca^{2+} and Mg^{2+} ions in the experimental group were measured by atomic absorption spectrometry (AAS, TAS-986, Zhengzhou Nanbei Instrument Equipment Co., Ltd., Zhengzhou, Henan Province, China) according to the published articles [38,39]. The precipitation ratio of Ca^{2+} and Mg^{2+} ions could be calculated by the following formula:

$$T = \frac{C_i - C_t}{C_i} \times 100\% \quad (1)$$

Here, T represented the precipitation ratio (%), namely the ratio of the mass/volume concentration), C_i the initial concentration (mg/L), and C_t the final concentration (mg/L).

2.6. Characterization of Precipitates

The mineral precipitates in the experimental group were taken out from the conical flask and thoroughly washed with distilled water, and then dried at room temperature. The filter membrane with pore size 0.22 μm was used to separate the minerals from the liquid culture medium in the control group without bacteria; no minerals were obtained. Thus, the study on the control group was terminated. The obtained precipitates in the experimental group were analyzed by X-ray diffraction (XRD, D/Max-RC, Rigaku Corporation, Japan) with the scanning angle (2θ) ranging from 10 to 60°, a step size of 0.02° and a count time of 8° min^{-1} . The XRD data were analyzed by Jade 6.5 software (Version 6.5, Materials Data Ltd., Livermore, CA, USA). The weight ratio of each mineral at different Mg/Ca molar ratios was calculated by Rietveld refinement in Materials Studio 8.0. The full width at half maximum (FWHM) of monohydrocalcite at Mg/Ca molar ratios 7 and 9 could be obtained by Jade 6.0. The mole percent of MgCO_3 in Mg-rich calcite was calculated using the following equation [40]:

$$x_{\text{MgCO}_3} = \frac{M_{\text{MgCO}_3}}{M_{\text{MgCO}_3} + M_{\text{CaCO}_3}} = -3.6396d_{104} + 11.0405 \quad (2)$$

Here, M_{MgCO_3} and M_{CaCO_3} represented the moles of MgCO_3 and CaCO_3 per formula unit of Mg-rich calcite, and d_{104} indicated the $d_{(104)}$ (Å) value of Mg-rich calcite.

To further test the mineral phase and the functional groups in/on the minerals, the precipitates were further analyzed by Fourier transform infrared spectroscopy (FTIR, Nicolet 380, Thermo Fisher Scientific Inc., Waltham, MA, USA) within the scanning range of 4000–400 cm^{-1} with a resolution of 4 cm^{-1} .

The morphology and elemental composition of the precipitates were determined by scanning electron microscopy (SEM, Hitachi S-4800, Japan Hitachi Company, Tokyo, Japan) with an X-ray energy dispersive spectrometer (EDS, EX-450, Japan Horiba, Tokyo, Japan).

To determine the stable carbon isotope composition, the obtained precipitates were pretreated using the method of Zhuang et al. [37], and then sent to the Center for Isotope Geochemistry and Geochronology (National Laboratory for Marine Science and Technology, Qingdao, China), and analyzed by a carbon isotope laser spectrometer (Picarro G2121-i, rPicarro Inc., Santa Clara, CA, USA) with the heating and phosphoric acid method.

The precipitates at Mg/Ca molar ratios 7 and 9 were also analyzed by a thermogravimetric analyzer (TGA/DSC1/1600LF, Mettler Toledo Co., Schwerzenbach, Switzerland) in the temperature range 50–1000 $^{\circ}\text{C}$ at a heating rate of 10 $^{\circ}\text{C min}^{-1}$.

The chemical characteristics of the mineral surface were analyzed by X-ray photoelectron spectroscopy (XPS, Thermo Scientific Escalab ESCALAB 250XI, Thermo Fisher Scientific, Waltham, MA, USA) fitted with a non-monochromatic Al-K α X-ray source. The survey (wide) spectra were collected from 1350 to 0 eV with a step size of 0.2 eV, and more detailed scans for elements Ca, O, C, N, S, and P were performed over the regions of interest. Avantage2.16 software (2.16, Thermo Fisher, Shanghai, China) was used to analyze the XPS spectra core-level lines for curve fitting. All spectra were referenced to the O $1s$ peak of carbonate at 530.9 eV [41].

2.7. Amino Acid Composition of EPS

EPS of *H. smyrnensis* WMS-3 bacteria were extracted with the heating method of Morgan et al. [42] and Zhuang et al. [37], then the obtained EPS solution was dried in a lyophilizer (FD-1A-50, Shanghai Bilang Instrument Manufacturing Co. Ltd., Shanghai, China) at -60°C under vacuum conditions, after that, the EPS powder was sent to Jiangsu Coastal Chemical Analysis & Technological Service Ltd. and analyzed by an amino acid analyzer (L-8900, Hitachi, Tokyo, Japan).

2.8. Analyses of Ultrathin Slices of *H. smyrnensis* WMS-3 Bacteria

Ultrathin slices of *H. smyrnensis* WMS-3 bacteria with a thickness of 70 nm were prepared with the method reported by Han et al. [36], and then observed by high-resolution transmission electron microscopy (HRTEM, JEM-2100, Japan Electronics Company, JEOL, Tokyo, Japan) [43–47], selected area electron diffraction (SAED) [48,49], scanning transmission electron microscope (STEM, Tecnai G2 F20, FEI, Hillsboro, OR, USA), and elemental mapping.

2.9. Fluorescence Intensity of Intracellular Ca^{2+} Ions

Fluorescence indicator Fluo-3 AM was used to mark intracellular Ca^{2+} ions of WMS-3 bacteria cultured at Mg/Ca molar ratios 0, 2, 5, 7, and 9, also including WMS-3 bacterial seed. At the same time, these above cells without being marked by Fluo-3 AM (acetoxymethyl ester form, Molecular Probes) were considered to be control groups. The detailed steps for the use of Fluo-3 AM were according to the method of Han et al. [50]. The fluorescence intensity was measured by a fluorescence spectrophotometer (FluoroMax-4, Horiba Jobin Yvon, France). Statistical analysis was performed by SPSS 21 software (Version 21.0, International Business Machines Corporation, Armonk, NY, USA).

3. Results and Discussions

3.1. 16S rDNA Identification of WMS-3 Bacteria

The 16S rDNA sequence of WMS-3 bacteria was detected to be 1449 bp in length and uploaded to the GenBank with an accession number MH425323. By BLAST analysis, WMS-3 bacteria shared 100% homology with a large number of bacteria belonging to the genera *H. smyrnensis*. The phylogenetic tree shown in Figure 1 indicates that the WMS-3 strain had the closest genetic relationship with *H. smyrnensis* species. Thus, the WMS-3 strain belongs to a species of *H. smyrnensis*.

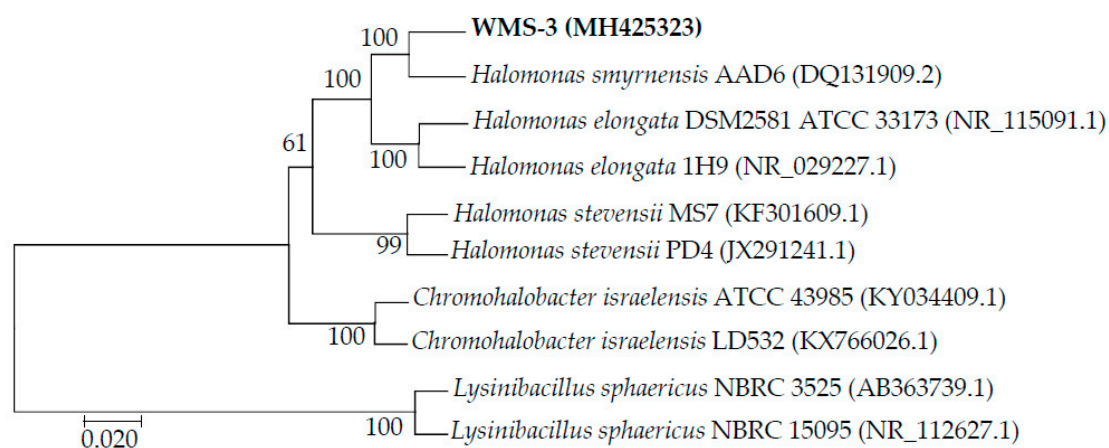


Figure 1. Phylogenetic tree of the *H. smyrnensis* WMS-3 bacteria constructed with neighbor-joining method based on 16S rDNA sequence alignment.

3.2. Characterization of *H. smyrnensis* WMS-3 Bacteria

3.2.1. Cell Morphology, Gram Staining, and Ammonia Test

The *H. smyrnensis* WMS-3 bacterium is about 2 μm in length, and 0.5 μm in width (Figure 2a). The result of Gram staining shows a red color (Figure 2b), indicating that *H. smyrnensis* WMS-3 bacteria are Gram-negative. It can be clearly seen that the liquid in the experimental group (the tube on the left in Figure 2c) is turbid due to the presence of *H. smyrnensis* WMS-3 bacteria, whereas the liquid in the control group (the tube on the right in Figure 2c) is transparent before adding the Nessler's reagent. After adding the Nessler's reagent, the color of the experimental group changed to yellowish-brown (the tube on the left in Figure 2d), and the control group (the tube on the right in Figure 2d) became yellow that is the color of the Nessler's reagent. Through these series of color changes, it can be concluded that the *H. smyrnensis* WMS-3 has the ability to release ammonia.

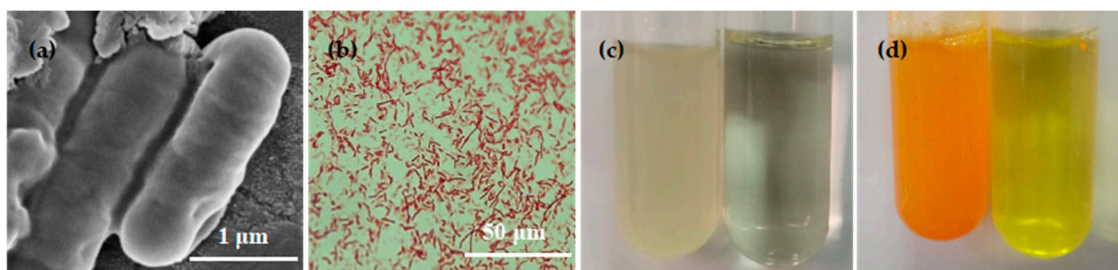


Figure 2. Morphology in SEM view (a), Gram staining in a biological microscope view (b), and ammonia test (c,d). (c) before adding the Nessler's reagent (d), after adding the Nessler's reagent. (left: the experimental group; right: the control group).

3.2.2. The Growth Curve of *H. smyrnensis* WMS-3 and pH Variation

It was not difficult to find from the growth curve of the *H. smyrnensis* WMS-3 bacteria under different salt concentrations that the optimum NaCl concentration was 3% (Figure 3a). As shown in Figure 3b, the growth curve of WMS-3 bacteria was divided into four periods: the delay/adaption phase (0–4 h), the logarithmic growth phase (4–50 h), the stationary phase (50–100 h), and the decline phase (100–453 h) [51]. The pH value of the experimental group (the green curve) eventually reached around 9.0, while that of the control group (the black curve) kept at 7.0 or so, almost unchanged (Figure 3b). The difference in pH value between the experimental and control group was significant ($p < 0.01$), further demonstrating the important role played by WMS-3 bacteria. In the time range 146–453 h, corresponding to the decline period of WMS-3 bacterial growth, the pH in the experimental group increased from 8.32 to 8.88, suggesting that the reasons for pH increase may be very complicated under the condition of lack of carbon and nitrogen sources. Han et al. [36,50,52] and Zhuang et al. [37] have reported that the reason for pH increase is not only related to the ammonia released by bacteria but also related to CA activity. Thus, the ammonium concentration and CA activity of WMS-3 bacteria was also analyzed to prove further whether ammonia and CA activity had a close relationship with an increase in pH values in the experimental group in this study.

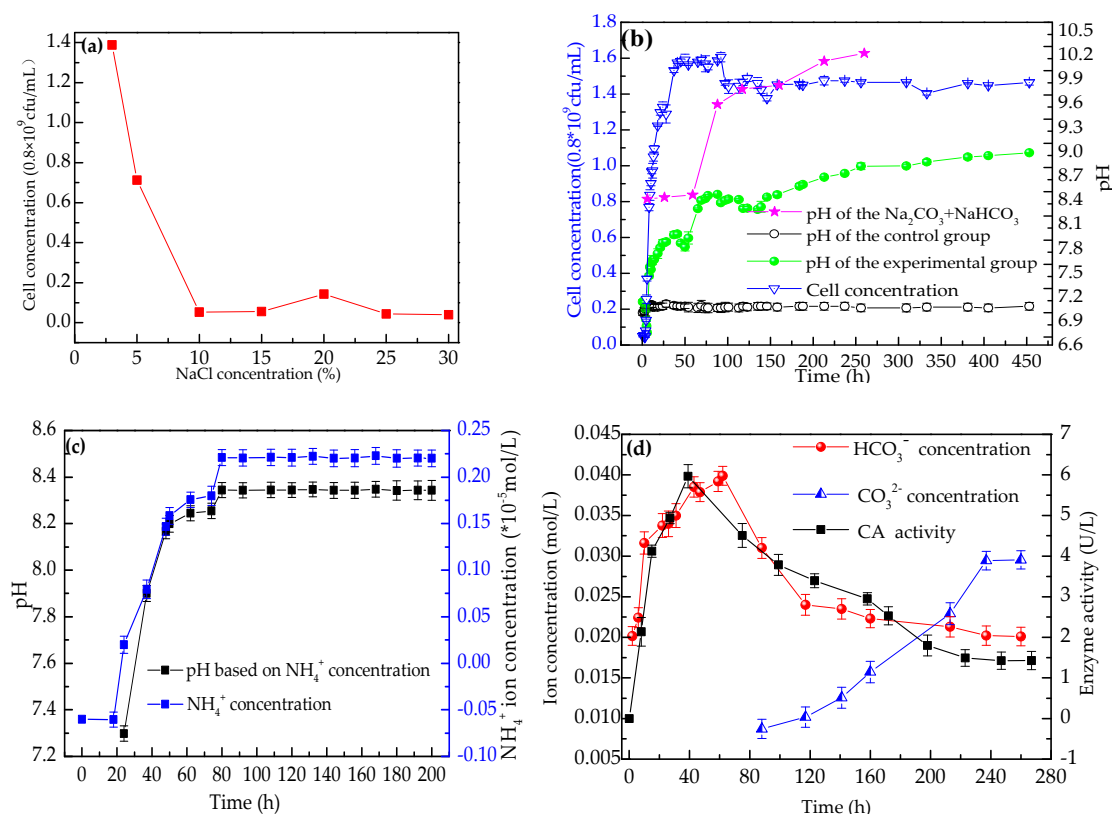


Figure 3. Physiological and biochemical characteristics of *H. smyrnensis* WMS-3 bacteria. (a) Growth curve of the *H. smyrnensis* WMS-3 bacteria at different NaCl concentrations after 24 h of cultivation; (b) Growth curve and pH changes; (c) NH_4^+ concentrations and pH curve based on NH_4^+ concentrations; (d) CA activity, and HCO_3^- , and CO_3^{2-} ion concentrations.

3.2.3. Ammonium Concentration and pH Value Based on the Concentration of Ammonium

According to the results in 3.2.1, ammonia could be released by WMS-3 bacteria, which would then be dissolved in the liquid medium to produce ammonium and hydroxyl ions. The chemical reaction would be as follows:



The amount of ammonia released by WMS-3 bacteria can be expressed in terms of ammonium concentration. In this study, the concentration of ammonium was almost zero before 24 h and increased sharply in the time range of 24–74 h, eventually reaching a stable state (Figure 3c). The pH value based on ammonium ion concentration increased from 7.3 to the maximum value 8.34 (Figure 3c), while that of the experimental group could reach about 8.9—much higher than the former 8.3 ($p < 0.01$). That is to say, the quantity of ammonia release by WMS-3 bacteria could not satisfy the requirement of pH increasing to 8.9, suggesting that there was something else affecting the pH increase besides ammonia in the experimental group. Our results are consistent with the conclusions reported by Han et al. [36,50,52] and Zhuang et al. [37]. Early, it is a general recognition that the ammonia released by bacteria is the main reason for the pH increase in an environment with abundant bacteria [50]. Now, there is a much better and more scientific explanation for why microbes cause pH to rise.

3.2.4. CA Activity and the Concentration of CO_3^{2-} and HCO_3^- Ions

CA enzymes have gained considerable attention for their potential use in CO_2 capture [53], and recently they have been used as a biocatalyst to sequester CO_2 through the transformation of CO_2 to HCO_3^- and CO_3^{2-} ions in the CaCO_3 mineralization process [54]. At present, a consensus that CA can accelerate the rate of carbonate mineral formation has been reached [55]. Based on this important role played by CA, as mentioned above, CA released by WMS-3 bacteria was also studied. In this study, CA activity sharply increased from almost zero to 5.97 U/L in the time range 0–39 h, and then slowly decreased from 6 U/L to 1.43 U/L in the time range 39–267 h (Figure 3d), that is to say, CA enzyme was released by WMS-3 bacteria. The most important point was that CA activity still existed in the decline stage of WMS-3 bacterial growth, indicating that maybe the pH increase in the decline stage was related to CA activity. CA can catalyze the hydration reaction of carbon dioxide to release bicarbonate and carbonate ions in the alkaline condition created by ammonia [37]. The reactions are listed as follows:



Since CA can catalyze the production of HCO_3^- and CO_3^{2-} ions, the concentration of HCO_3^- and CO_3^{2-} ions were also measured in this study. The concentration of HCO_3^- ion first increased to 0.04 mol/L at 62 h and then decreased slowly in the time range 62–117 h, and finally kept almost constant at 0.02 mol/L in the time range 117–260 (Figure 3d). The concentration of CO_3^{2-} ions could not be detected before 88 h, and then sharply increased to 0.029 mol/L at 237 h, and at last, reached a stable state in the time range 237–260 h (Figure 3d).

Han et al. [36,50,52] and Zhuang et al. [37] have reported that the resulting HCO_3^- and CO_3^{2-} ions produced by the CA enzyme could lead to an increase in pH values in the culture medium. Thus, according to their methods, ($\text{NaCO}_3 + \text{NaHCO}_3$) solutions were prepared, corresponding to the concentrations of HCO_3^- and CO_3^{2-} ions, and the pH values based on the ($\text{NaCO}_3 + \text{NaHCO}_3$) solutions were also measured. The result showed that the pH values based on the ($\text{NaCO}_3 + \text{NaHCO}_3$) solutions increased from 8.3 to 10.12 during the period 0–260 h (Figure 3b), indicating that the changes in the concentration of HCO_3^- and CO_3^{2-} ions also influenced the pH in the medium. Therefore, an increase in the pH values in the experimental group resulted from the presence of ammonia and the catalysis of CA, consistent with the results reported by Han et al. [36,50,52] and Zhuang et al. [37]. It could be there are other factors that increase pH, which need to be explored further.

3.3. Changes in the Concentration of Ca^{2+} and Mg^{2+} Ions

Precipitates were produced in the experimental group, whereas no minerals were obtained in the control group. Thus, from this step onwards, the control group was not studied anymore.

The concentrations of Ca^{2+} ions in the experimental group at Mg/Ca ratios 0, 2, 5, 7, and 9 showed the same trend, and decreased continuously from the original 400 mg/L to 142.74, 151.18, 159.12, 161.73, and 182.31 mg/L in the time range from 0–21 days, respectively (Figure 4a). The precipitation ratio (% from the ratio of the mass/volume concentration) of Ca^{2+} ion was 64.32%, 62.20%, 60.22%, 59.57%, and 54.42% at the Mg/Ca molar ratios of 0, 2, 5, 7, and 9, respectively (Figure 4c). The Mg^{2+} ion concentration changed a little (Figure 4b), and the precipitation ratio of Mg^{2+} ion was 6.69%, 7.10%, 7.74%, and 8.09% at Mg/Ca molar ratios of 2, 5, 7, and 9, respectively (Figure 4d).

In this study, the Ca^{2+} ion concentration was 0.01 M, far below the concentration of the Mg^{2+} ion, while the precipitation ratio of the Ca^{2+} ion was much higher than that of the Mg^{2+} ion, suggesting that it was much more difficult for Mg^{2+} ions to participate in the bio-precipitation process than Ca^{2+} ions. It has been reported that the hydrated cations, such as $\text{Mg}(\text{H}_2\text{O})_6^{2+}$ and $\text{Ca}(\text{H}_2\text{O})_6^{2+}$, needed to have the hydrated membrane surrounding them removed if they are to form $\text{Mg}-\text{CO}_3^{2-}$ and $\text{Ca}-\text{CO}_3^{2-}$ pairs [56]. Moreover, the energy required for the dehydration of $\text{Mg}(\text{H}_2\text{O})_6^{2+}$ is 351.8 kcal/mol, higher than that of $\text{Ca}(\text{H}_2\text{O})_6^{2+}$ (264.3 kcal/mol) under standard conditions (298 K, 1atm) [57]. Thus, it is much more difficult for Mg^{2+} ions to form magnesium carbonate minerals, due to the higher energy required for the dehydration. There are also other opinions as to why it is difficult for the Mg^{2+} ion to be precipitated as magnesium carbonate minerals. Mg^{2+} ions with no hydrated membrane in dry formamide still do not form magnesium carbonate crystals, and the reason given was that the lattice limitation resulting from the spatial configuration of CO_3^{2-} groups prevented Mg^{2+} and CO_3^{2-} ions from forming crystalline structures [58]. There are many factors affecting the mineralization of the Mg^{2+} ion, which need to be explored.

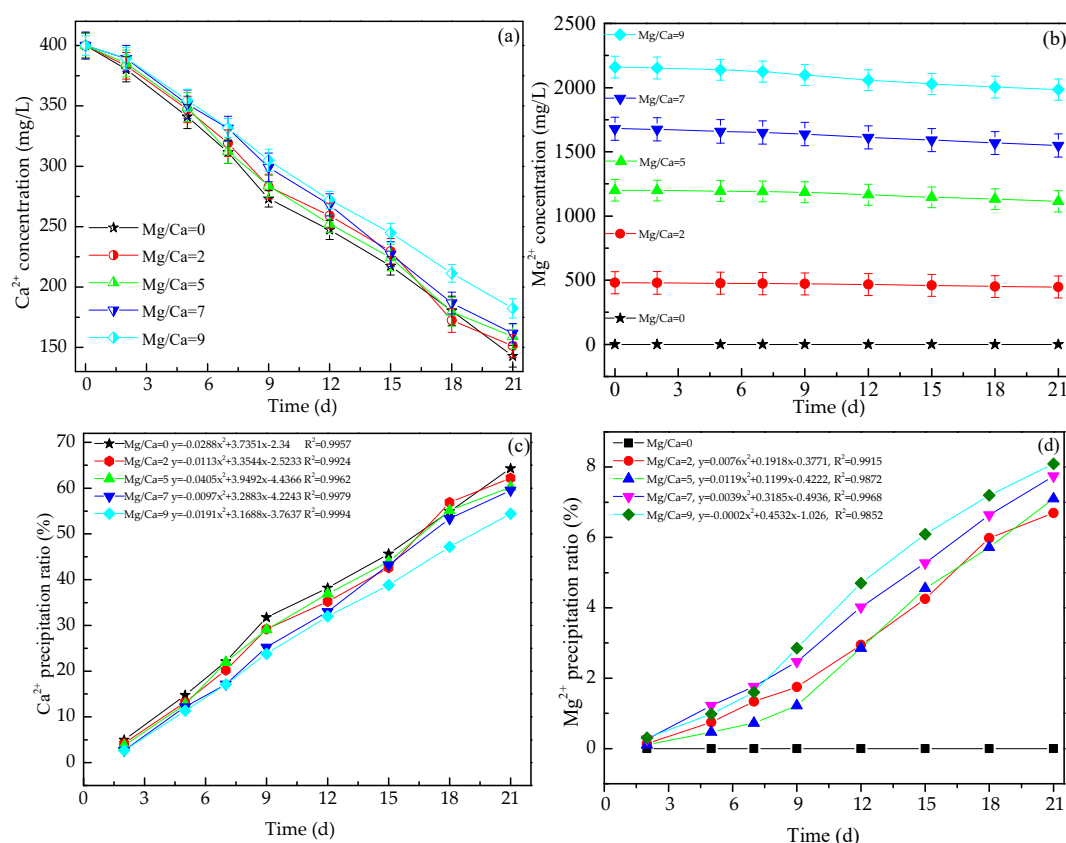


Figure 4. Changes of Ca^{2+} concentration (a), Mg^{2+} concentration (b), Ca^{2+} precipitation ratio (c), and Mg^{2+} precipitation ratio (d).

3.4. Characterization of the Biominerals

3.4.1. XRD Analyses

In this study, no precipitates were obtained in the control group; thus, only the experimental group needed to be studied. At Mg/Ca = 0, the biomineral was only calcite, syn (PDF-# 05-0586) (Figure 5 and Figure S1a). At Mg/Ca = 2, Mg-rich calcite (PDF-# 43-0697), aragonite (PDF-# 41-1475), and monohydrocalcite (PDF-# 29-0306) minerals were obtained (Figure 5); the weight percent of Mg-rich calcite, aragonite and monohydrocalcite was 62.93%, 0.01%, and 37.06%, respectively (Figure S1b); 9.09% MgCO₃ (molar ratio) was present in the Mg-rich calcite (Figure 5). At Mg/Ca = 5, aragonite (PDF-# 41-1475), monohydrocalcite (PDF-# 29-0306), and hydromagnesite (PDF-# 25-0513) minerals were found (Figure 5); the weight ratio of hydromagnesite was 61.82%, monohydrocalcite 24.38%, and aragonite only 13.80% through Rietveld refinement (Figure S1c). At Mg/Ca molar ratios 7 and 9, the minerals were monohydrocalcite (PDF-# 29-0306) and hydromagnesite (PDF-# 25-0513) (Figure 5). When the Mg/Ca molar ratio changed from 7 to 9, the weight percent of hydromagnesite decreased from 76.15% to 9.99%, and that of monohydrocalcite increased from 23.85% to 90.01% (Figure S1d,e). What is more, the FWHM (°) of monohydrocalcite at Mg/Ca = 7 was higher than that at Mg/Ca = 9 (Table S1), indicating that monohydrocalcite had a much better crystalline structure when the Mg/Ca molar ratio increased from 7 to 9.

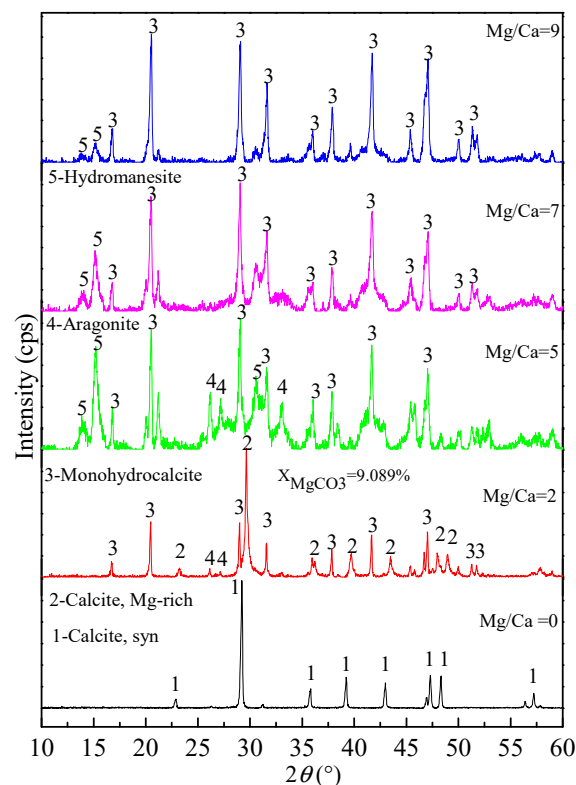


Figure 5. XRD analyses of biominerals cultured for 30 days.

Monohydrocalcite had previously only been found in fresh-water or terrestrial environments before researchers documented the presence of submarine monohydrocalcite [28]. In this study, the formation of monohydrocalcite induced by WMS-3 bacteria was in a liquid medium with 3% NaCl, which is similar to seawater, also demonstrating the fact that monohydrocalcite can be formed in an environment rich in salt in the lab. Mg plays an important role in the formation and stability of monohydrocalcite [59]. It has been reported that the crystalline monohydrocalcite can be easily prepared at a certain Mg/Ca molar ratio (>1), and that a small amount of Mg²⁺ ion can be incorporated

into the lattice structure of monohydrocalcite to stabilize the crystal water [60,61]. In this study, the concentration of the Mg^{2+} ion slowly decreased (Figure 4b,d), maybe due to the incorporation of Mg^{2+} ion into the monohydrocalcite crystals besides the formation of hydromagnesite. However, Han et al. [36,50] used *Bacillus licheniformis* DB1-9 and *Bacillus subtilis* J2 bacteria to induce the formation of biominerals at different concentrations of Mg^{2+} ions, and the obtained mineral is aragonite and not monohydrocalcite in the presence of Mg, a different result from ours. Moreover, Han et al. [52] found that the obtained mineral is monohydrocalcite when using the halophile *Staphylococcus epidermis* Y2 in a medium with higher concentrations of Mg^{2+} ions, the same as ours. Thus, a very important question has arisen: since Mg is present in the environment and plays an important role in monohydrocalcite formation, why is the resulting mineral not necessarily monohydrocalcite? In our opinion, the formation of monohydrocalcite is not only related to Mg but also closely tied to the microbial species. It has been reported that the release of Mg^{2+} ions can induce the phase transformation of monohydrocalcite to anhydrous aragonite in aqueous systems [62]. Thus, it could be inferred that some bacteria would make more Mg^{2+} ions be incorporated into carbonate minerals than other bacteria. In this case, the former was conducive to the formation of monohydrocalcite and the latter to the formation of aragonite.

3.4.2. FTIR Analyses

The characteristic bands of calcite are 712, 875, 1421, and 2514 cm^{-1} [36], and those of aragonite are 710, 856, 1082, and 1475 cm^{-1} [63]. 700, 766, 872, 1060, 1401, and 1492 cm^{-1} are the characteristic bands of monohydrocalcite [63], and the characteristic bands 592, 796, 854, 877, 1426, 1488, 3649 belong to hydromagnesite [64].

The bands 712, 875, 1421, and 2514 cm^{-1} of minerals at the Mg/Ca ratio 0 indicate the presence of calcite (Figure 6a); at Mg/Ca = 2, besides the bands 712, 875, and 2514 cm^{-1} of calcite (Mg-rich), there are the bands 700, 1060, 1401, and 1492 cm^{-1} of monohydrocalcite; 712 cm^{-1} and 1492 cm^{-1} also belong to aragonite (Figure 6b). At Mg/Ca = 5, besides the characteristic bands of monohydrocalcite (700, 766, 872, and 1492 cm^{-1}), the bands 710 cm^{-1} and 1082 cm^{-1} prove the formation of aragonite (Figure 6c). 592, 796, and 1426 cm^{-1} indicate the presence of hydromagnesite (Figure 6c). At Mg/Ca = 7 and 9, the characteristic bands prove that the minerals are monohydrocalcite (700, 766, 872, 1492 cm^{-1}) and hydromagnesite (592, 796, 1426 cm^{-1}) (Figure 6d,e). The mineral phases obtained by FTIR are consistent with the results of XRD. Moreover, besides these characteristic bands of minerals, organic functional groups are also found to be present in/on the minerals, including C=O (1620 cm^{-1} , 1638 cm^{-1}) [36,65] and C–O–C (1068 cm^{-1}) [66] (Figure 6a–e).

Previously, some scholars have proposed that the C–O–C group plays an important role in biomineralization [66]. Our results shown in Figure 6a–e are further confirming the previous opinion. The C–O–C functional group present in/on the minerals also confirms the biogenesis of these minerals. Some functional groups associated with biomacromolecules from bacteria could play important roles in the formation of the peculiar morphology of the biominerals in the biomineralization process. It has been reported that F68, composed of predominant –C–O–C– and a terminal –OH groups, was used as a model organic additive to study the biomimetic mineralization of calcite, and the results showed that the terminal hydroxyl group in F68 had a negligible contribution to the morphogenesis of calcite due to its much lower content, and the –C–O–C– groups (ether or glycosidic group) contributed to the formation of special calcite, like the elongated calcite and the bundle-shaped calcite [67]. In our study, the –C–O–C– groups indeed present in/on the minerals (Figure 6a–e) has been confirmed, and the –C–O–C– groups would also result in some changes in the morphology of biominerals according to Zhou's opinion. Thus, the morphology and elemental composition of the biominerals was also studied.

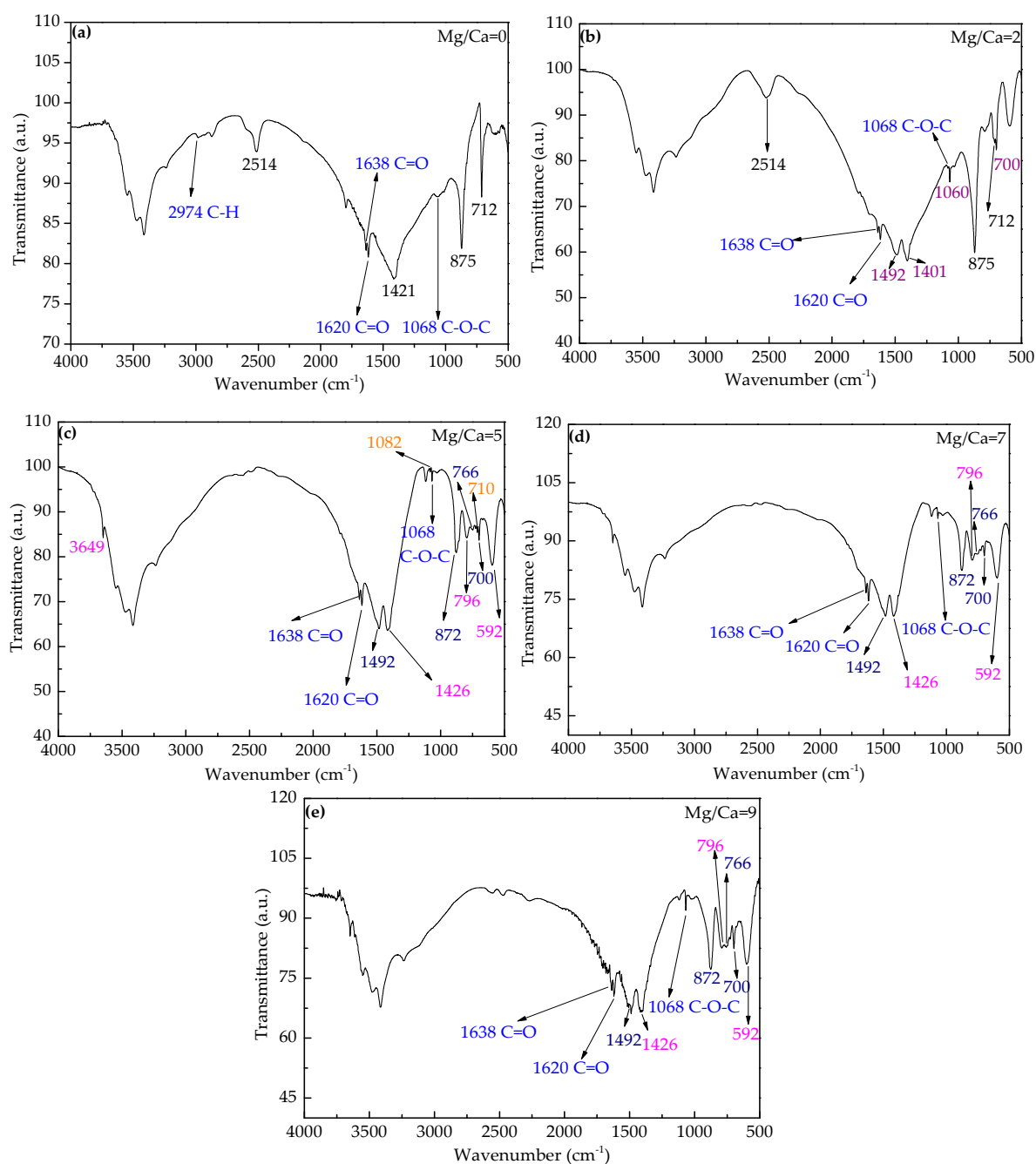


Figure 6. FTIR analyses of the biomaterials cultured for 30 days. (a–e) represents the minerals cultured at Mg/Ca ratios of 0, 2, 5, 7 and 9, respectively.

3.4.3. Morphology and Elemental Composition of the Biomaterials

Biogenic minerals tend to have a wide range of morphologies compared to physicochemical precipitates [68]. The basic form of the abiotic calcite is always a rhomb [37], while the biotic calcite at a Mg/Ca ratio of 0 in this study showed several morphologies, including cauliflower (Figure 7(a1)), elongate (Figure 7(a3)) and dumbbell shapes (Figure 7(a4)). In addition, it would appear that some bacteria lived within cavities on the mineral surface (Figure 7(a2)). The elements of the mineral in Figure 7(a4) include Ca, C, O, P, and S (Figure 7(a5)). Ca, C, and O elements are within the mineral calcite, and P and S elements may have come from the WMS-3 bacteria, bacterial metabolites, or the organic substances in the culture medium.

At $Mg/Ca = 2$, the surface of the spheroidal (Figure 7(b1,3)) and dumbbell-shaped minerals (Figure 7(b4)) are different from the spheroidal mineral in Figure 7(b2); the former is composed of a large number of nanometer-scale particles with no regular shape while the latter consist of many larger more regular-shaped minerals. The mineral in Figure 7(b3) contained Ca, C, O, P, S, and Mg elements (Figure 7(b5)). The origin of the Ca, C, O, P, and S is the same as the above, and Mg is from the culture medium. Compared with the Mg/Ca ratio 0, the morphology and elemental composition of minerals at Mg/Ca ratio 2 changed considerably, demonstrating the important role played by Mg.

At $Mg/Ca = 5$, there are dumbbell-shaped minerals composed of many crystallites in the shape of a petal (Figure 7(c1)), spheroidal minerals covered with minute rectangular crystallites (Figure 7(c2)), irregular minerals bearing abundant holes where likely bacteria once lived (Figure 7(c3)), and elongate minerals (Figure 7(c4)). The elongate minerals contain Ca, C, O, P, S, and Mg elements (Figure 7(c5)), and the origin of all these elements is the same as the above.

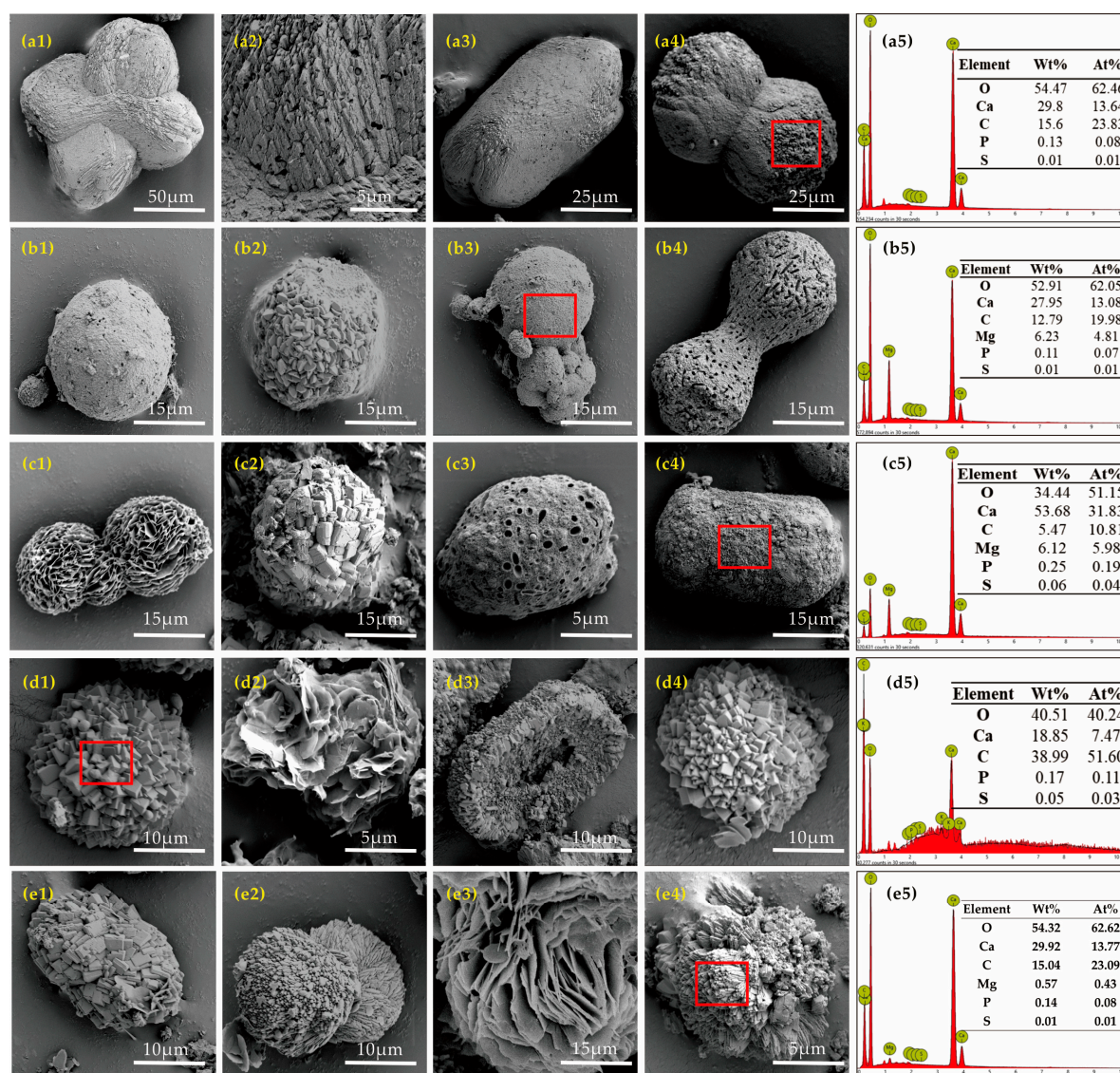


Figure 7. SEM and EDS analyses of minerals cultured for 30 days. (a–e), Mg/Ca molar ratios 0, 2, 5, 7, and 9, respectively. The red square shows the area analyzed by EDS.

At $Mg/Ca = 7$, the spheroidal minerals (Figure 7(d1,4)) and elongate minerals (Figure 7(d3)) are all covered with many minute rectangular crystallites. The outer shell of the elongate minerals is composed by larger rectangular crystals, while the inner part consists of smaller rectangular crystals

(Figure 7(d3)), indicating that the nucleation rate of minerals within the elongate mineral was much quicker than that of minerals located on the outer surface. The elements of the spheroidal minerals (Figure 7(d1)) include Ca, C, O, P, and S, and the origin of these elements is the same as the above. Too little to be detected perhaps is the reason for the absence of Mg in the EDS analyses. Besides the above morphology, petal-shaped minerals similar to that in Figure 7(c1) could also be observed (Figure 7(d2)).

At Mg/Ca = 9, there are elongate minerals (Figure 7(e1)), dumbbell-shaped minerals (Figure 7(e2)), and irregular-shaped mineral aggregates (Figure 7(e4)). The aggregates contain Ca, C, O, P, S, and Mg elements (Figure 7(e5)), and the origin of all these elements is the same as the above. The flower-shaped or petal-shaped mineral is still present in this culture system (Figure 7(e3)).

In brief, the diversity of morphology, complicated elemental composition, and bacteria present within holes in the minerals (Figure 7(a2), (b1,4), and (c3)) further proved that these resulting minerals were biogenic, not abiogenic. Researchers have many different views on whether minerals are biogenic according to the typical morphology. Some researchers have suggested that spheroidal and dumbbell shapes reflect their microbial origin and may serve as biosignatures in the rock record [69]. However, other researchers have disagreed and proposed that minerals with such structures can also be produced under abiogenic culture conditions [70]. Therefore, it is necessary to use other detection methods, not only the morphology, to determine whether minerals are biogenic or not.

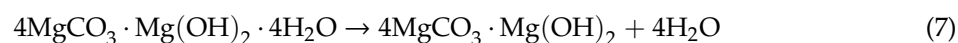
3.4.4. Stable Carbon Isotope Composition of the Biominerals

Microorganisms can utilize the carbon source in the medium to produce metabolites, such as different kinds of organic acid and large amounts of carbon dioxide. The metabolite carbon dioxide is different from atmospheric carbon dioxide—the former originates from organic substances, and the latter comes from the inorganic atmosphere. The stable carbon isotope values of mineral formed by metabolite carbon dioxide produced by chemoheterotrophic microorganisms would likely be more negative than those of mineral formed via atmospheric carbon dioxide [71]. In this study, the $\delta^{13}\text{C}$ values of the biotic carbonate minerals ranged from -16.91‰ to -17.91‰ (Table S2), more negative than that of atmospheric CO_2 ($\delta^{13}\text{C}$, -8‰) [72], but similar to that of beef extract (-18.4‰) and tryptone (-21.3‰) reported by Zhuang et al. [37]. Thus, the more negative stable carbon isotope values of the minerals produced in our experiments further confirms their biogenesis.

Sánchez-Román et al. [71] used different aerobic bacterial strains to induce the formation of Mg-rich carbonates at aqueous Mg/Ca ratios (2 to 11.5), and found that the $\delta^{13}\text{C}$ values for hydromagnesite, huntite, high Mg-calcite, and dolomite ranged from -26.8 to -18.2‰ . They interpreted this as proving that the carbon of the microbial carbonate precipitates was derived from the yeast extract and proteose peptone (-23.8 and -24.1‰ , respectively). Thus, microbial metabolism can strongly influence the carbon isotope composition of these carbonate biominerals, and the more negative $\delta^{13}\text{C}$ values proves their biogenesis.

3.4.5. Thermogravimetry-Derivative Thermogravimetry (TG-DTG) and Differential Scanning Calorimetry (DSC) Analyses of Monohydrocalcite at Mg/Ca Molar Ratios 7 and 9

To compare the thermal stability of monohydrocalcite between Mg/Ca ratio 7 and 9, TG-DTG and DSC analyses were performed. Whether the presence of hydromagnesite could make the TG-DTG and DSC results of monohydrocalcite hard to interpret was an issue that confused us. It has been reported that hydromagnesite ($4\text{MgCO}_3 \cdot \text{Mg}(\text{OH})_2 \cdot 4\text{H}_2\text{O}$) can undergo endothermic breakdown from 200 °C to 550 °C [73]. The thermal decomposition of hydromagnesite is described by the following reactions:



That is to say, hydromagnesite could be decomposed thoroughly before the temperature increases to 700–800 °C. It has also been reported that by the thermal dehydration observed in the range from 400 to 560 K, monohydrocalcite produces a calcite phase preferentially [74]. In general, the decomposition temperature of calcite is higher, 700–800 °C at a heating rate of 10 °/min [37]. Therefore, the thermal decomposition characteristics of monohydrocalcite are different from that of hydromagnesite.

From the TG curve, two obvious mass loss phases can be discerned: one was at about 210 °C and the other 780–90 °C (Figure 8a). The first mass loss phase represents the loss of crystalline water in the minerals monohydrocalcite and hydromagnesite, also overlapping the process of thermal dehydroxylation of dehydrated hydromagnesite [74], and the second indicates the thermal decomposition of the dehydrated monohydrocalcite [37].

There are also two obvious weight loss phases in Figure 8b: the first weight loss phase is in the range of 190–210 °C, resulting from the loss of crystalline water from monohydrocalcite and hydromagnesite and the thermal dehydroxylation of dehydrated hydromagnesite; the second weight loss phase is in the temperature range 700–800 °C, due to the decomposition of the dehydrated monohydrocalcite.

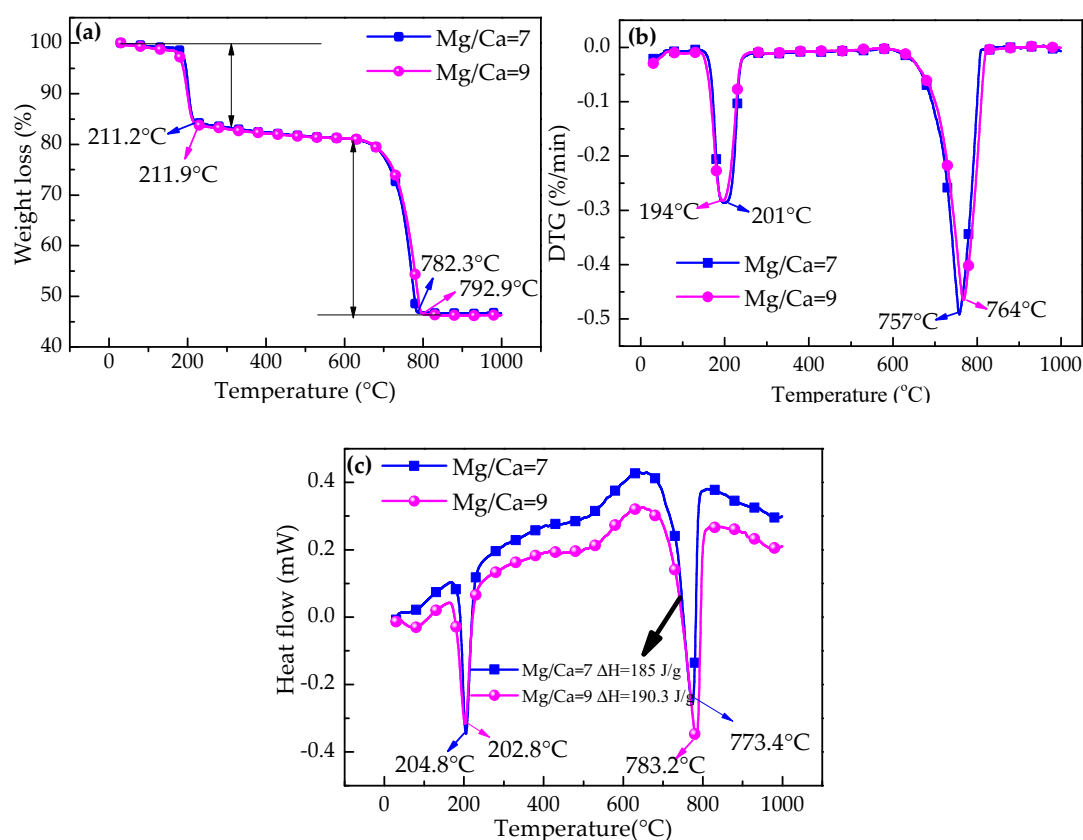


Figure 8. Thermogravimetry (TG) (a), differential thermogravimetry (DTG) (b), and differential scanning calorimetry (DSC) (c) analyses of minerals induced by *H. smyrnensis* WMS-3 bacteria cultured for 30 days at a heating rate of 10 °C min⁻¹.

The DTG results show that there is a great difference in the second peak temperature: 764 °C is the thermal decomposition temperature of the dehydrated monohydrocalcite at Mg/Ca ratio 9, higher than 757 °C of that at Mg/Ca ratio 7 (Figure 8b). Thus, the dehydrated monohydrocalcite at the Mg/Ca ratio of 9 has a higher thermal stability than that at the Mg/Ca ratio of 7. It has been reported that in the decomposition process of monohydrocalcite, vaterite can be formed sometimes, and the vaterite nucleus could be slowly transformed into calcite crystals; moreover, the formation of vaterite has a relationship with Mg content [74]. It could be that more vaterite would be formed in the decomposition process of monohydrocalcite at an Mg/Ca ratio of 7 due to the presence of a higher

content of hydromagnesite, which determines the lower thermal stability shown in the second weight loss step. Of course, this is just speculation; further tests are needed. Monohydrocalcite at different Mg/Ca molar ratios exhibits different thermal behaviors, likely due to the different morphologies and crystallinities.

DSC results (Figure 8c) show that 1 g of the dehydrated monohydrocalcite at an Mg/Ca ratio of 9 needed 190.3 J to decompose, higher than the 185 J for that at an Mg/Ca ratio of 7; moreover, 783.2 °C is the second peak temperature for the decomposition of the dehydrated monohydrocalcite at an Mg/Ca ratio of 9, also higher than 773.4 °C for that at an Mg/Ca ratio of 7. The above DSC results also reveal that the thermal stability of the dehydrated monohydrocalcite at an Mg/Ca ratio of 9 is higher than that at an Mg/Ca ratio of 7. The reason may be closely related to the higher crystallinity of monohydrocalcite at an Mg/Ca ratio of 9 (Table S1). From the above, it appears that Mg^{2+} ions could promote the formation of monohydrocalcite under the influence of WMS-3 bacteria. The changes in the crystalline structure and thermal decomposition process of monohydrocalcite are in need of further study.

3.4.6. Characterization of Surface Chemistry with XPS

XPS analysis was performed to determine the surface heterogeneity of the biomineral further, facilitating the understanding of the important role played by some organic substances in the formation of these carbonate precipitates. Through XPS experiments, the atomic composition can be obtained by analyzing the characteristic peaks of binding energy through high-resolution scan of the elements [75]. The results of XPS clearly show the presence of C, O, Ca, N, S, and P on the surface of the biomineral induced by WMS-3 (Figure 9a–g).

As shown in Figure 9b, two new peaks at 342.7 and 346.3 eV are assigned to Ca_{2p} [76]. The C_{1s} peak (Figure 9c) at 280.86 eV indicates that carbon is bound only to carbon and hydrogen (C–(C, H)), and the peak at 284.86 eV illustrates that carbon is singly-bound to oxygen or nitrogen (C–(O, N)) from ethers, alcohols, amines, and/or amides [77]. Nitrogen appears at a binding energy of 395.56 eV (Figure 9d), due to the presence of amine or amide groups of proteins [41]. The oxygen peak (O_{1s}) at 527.11 eV (Figure 9e) indicates that oxygen is double bonded with carbon or phosphorus (C=O or P=O) from carboxylic acids, carboxylates, esters, carbonyls, amides, or phosphoryl groups [78]. Phosphorus is found at a binding energy of 128.96 eV (Figure 9f), attributed to phosphate groups [78]. The peak fitting results (Figure 9g) reveal that S_{2p} is contributed by the $S_{2p}^{3/2}-H$ at 162.81 eV [79]. The carboxyl groups, phosphoryl groups, and other groups mentioned above can also provide metal cation binding sites [80]. The deconvolution for high-resolution O_{1s} spectra further reveals that the binding energy of O assigned as O=C–O group shifts from 531.5 [41] to 527.11 eV after the adsorption of Ca^{2+} and Mg^{2+} (Figure 9e), confirming that interactions between carboxyl groups with Ca^{2+} and Mg^{2+} ions have occurred. Moreover, the deconvolution for high-resolution P_{2p} spectra indicate that the binding energy assigned as the phosphoryl group shifted from 133.4 [78] to 128.96 eV due to Ca^{2+} and Mg^{2+} adsorption (Figure 9f). These functional groups may have come from WMS-3 bacteria and bacterial metabolites. Thus, XPS results further reveal the important role played by WMS-3 bacteria in the formation of biominerals.

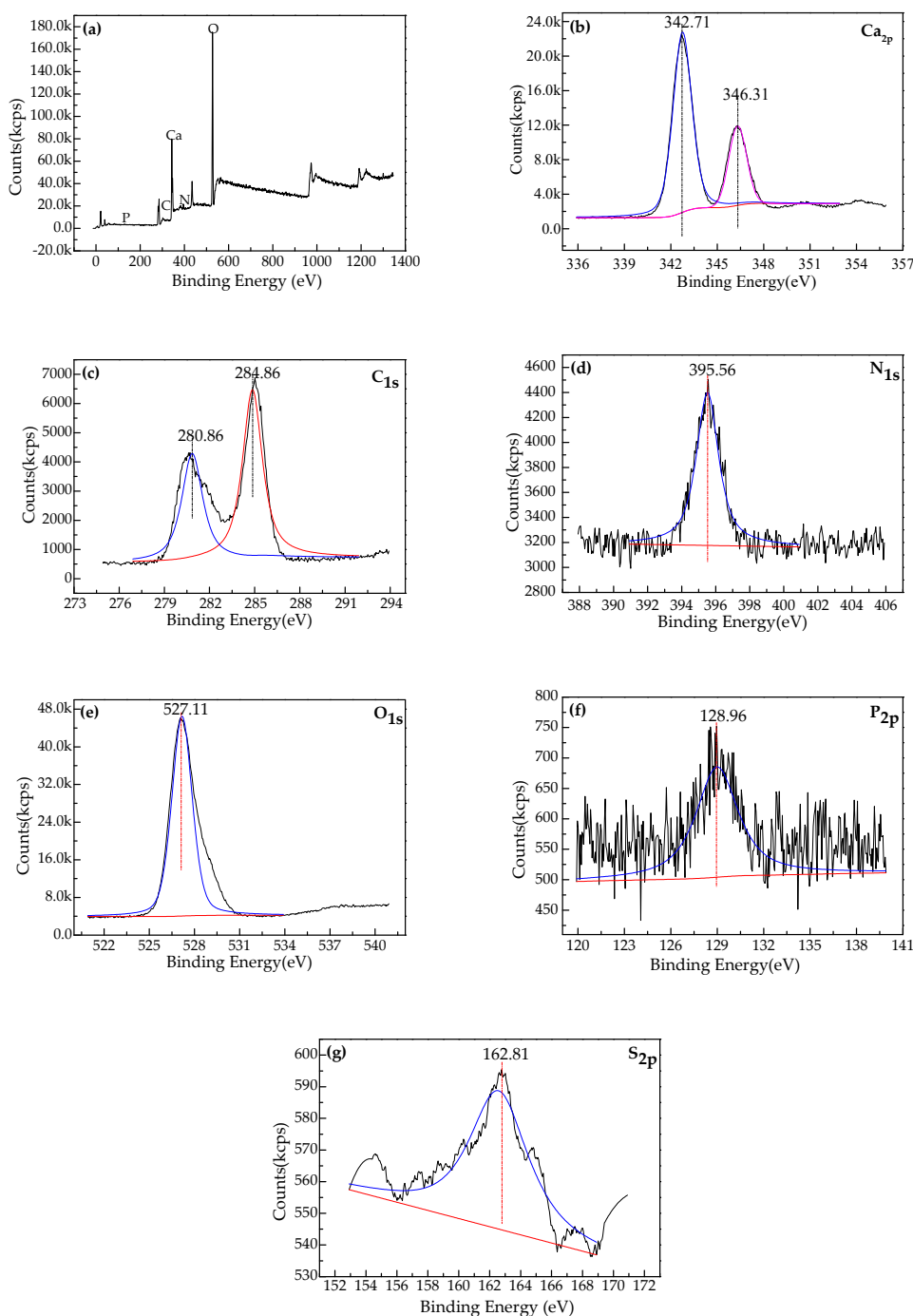


Figure 9. X-ray photoelectron spectroscopy (XPS) broad survey of minerals at Mg/Ca molar ratio of 9 (a) and high-resolution of Ca (b), C (c), N (d), O (e), P (f), and S (g).

3.5. Intracellular Biomineralization of *H. smyrnensis* WMS-3 Bacteria

The bacterial seeds cultured in a medium without any Ca^{2+} and Mg^{2+} ions were set as the control, and the bacteria growing in a medium with Mg/Ca ratios 0, 2, 5, 7, and 9 were considered as the experimental groups. The growth of the bacterial seeds was normal, and the EPS and cell wall could be clearly observed; moreover, no nanometer-scaled dark inclusions were present inside the cells (Figure 10(a1–3)). However, in the environment with different concentrations of Ca^{2+} and Mg^{2+} ions, some cells were deformed and dark inclusions with different sizes (marked with yellow circles and purple arrows) appeared inside the cells (Figure 10b–f), revealing a great difference in the intracellular

biomineralization between the control and experimental group. In our opinion, the deformation of cells was due to the consequence of the osmotic pressure produced by different concentrations of calcium and magnesium ions. WMS-3 bacteria can tolerate up to 3% NaCl, and the cells dehydrated and died when NaCl concentration increased (Figure 3a). In the same way, Ca^{2+} and Mg^{2+} ions can travel down the ion channel into the cell [36,37,50], causing the cell to dehydrate, which may be the cause of cell deformation. Ca^{2+} and Mg^{2+} ions that entered the cell's interior could have accumulated in a region to form a series of nanoscale dark inclusions, just as too many Ca^{2+} ions eaten by humans could form stones in a particular part of the body. However, the intracellular inclusions have no crystalline structure as shown by the lack of diffraction spots and circles in the SAED images (Figure 10(g1–5)).

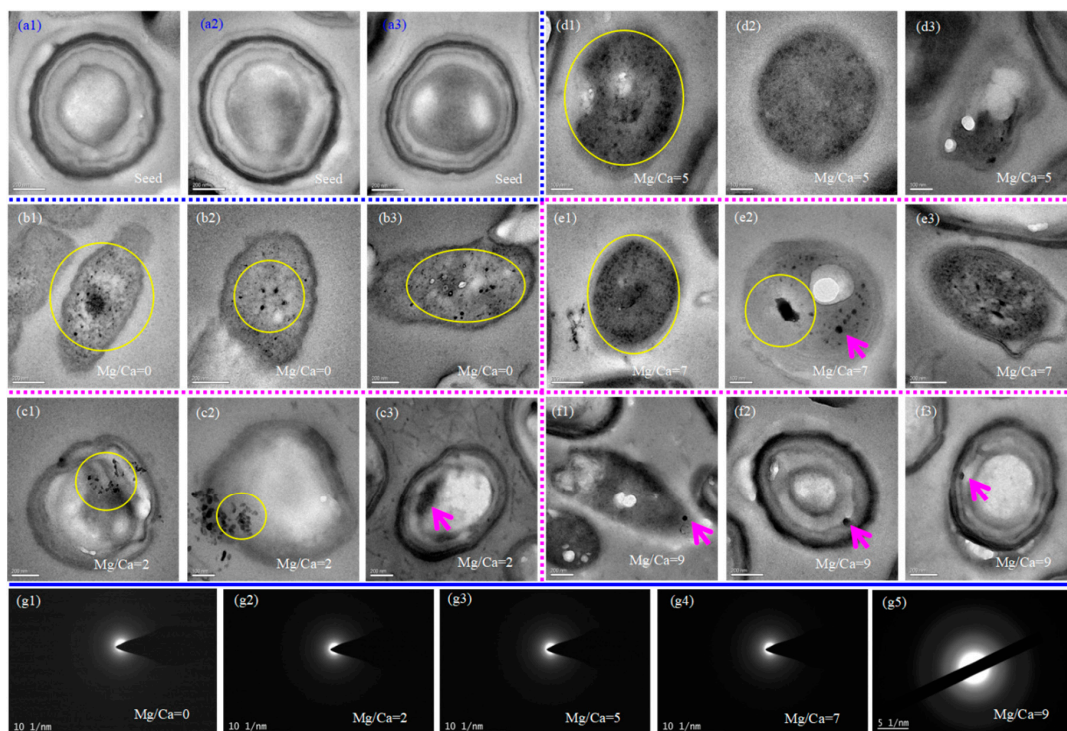


Figure 10. High-resolution transmission electron microscopy (HRTEM) and selected area electron diffraction (SAED) analyses of intracellular biomineralization of *H. smyrnensis* WMS-3 bacteria. (a), Bacterial seed; (b–f), Bacteria at Mg/Ca molar ratios of 0, 2, 5, 7, and 9, respectively; (g1–5), SAED analyses of the intracellular inclusions of bacteria at Mg/Ca molar ratios 0, 2, 5, 7, and 9, respectively. (The arrows and the circles represent the location of biomineralization).

Studies of intracellular biomineralization have been rarely reported due to the limitation of the technology. Couradeau et al. [81] found that a cyanobacterium growing in modern microbialites in Lake Alchichica (Mexico) contains intracellular amorphous carbonate inclusions with calcium, magnesium, strontium, and barium elements. Recently, *Candidatus* Gloeomargarita lithophora, a species of deep-branching cyanobacteria, has been reported to contain amorphous Ca-rich carbonates inside the cell [82]. There are also some microorganisms that can form intracellular minerals with crystalline structures. Keim et al. [83] found that some magnetosomes containing single prismatic magnetite crystals are present in uncultured marine magnetotactic bacteria. Thus, some intracellular biomineralization products have amorphous structures, and other intracellular biominerals could be crystalline. The reported amorphous intracellular inclusions are mostly amorphous calcium carbonate (ACC), and the bacteria themselves are commonly cyanobacteria; where the intracellular minerals are magnetite, the bacteria are always magnetotactic bacteria. As for *H. smyrnensis* bacteria, intracellular biomineralization has rarely been reported. The amorphous intracellular inclusions formed in *H. smyrnensis* bacterial cells may have been a protection mechanism for survival in the face of adversity.

Perri et al. [84] suggested that intracellular precipitates could be permineralised viruses. The study of intracellular biomineralization has only just begun, and its mechanism still needs to be explored further.

3.6. EPS Acting as the Nucleation Sites

There were no nanometer-scale minerals detected on/in the EPS of WMS-3 bacteria in a liquid medium without any Ca^{2+} and Mg^{2+} ions (Figure 10(a1–3)), while some nanometer-scale minerals appeared in/on EPS (marked by the blue arrows and yellow circles) when WMS-3 bacteria were in a medium with abundant Ca^{2+} and Mg^{2+} ions (Figure 11a–d). Moreover, some cells were completely surrounded by a large number of nanoscale particles in/on the EPS (Figure 11(d2)). The nanoscale particles marked by a yellow circle in Figure 11(c3) were proved to be monohydrocalcite by HRTEM analysis (Figure S2a) due to the presence of (312), (302), (113), and (103), and the minerals also marked by a yellow circle in Figure 11d3 were also confirmed to be monohydrocalcite by SAED analysis (Figure S2b) because of the occurrence of (111), (211), and (302); thus, further revealing that EPS of WMS-3 bacteria could act as the nucleation sites.

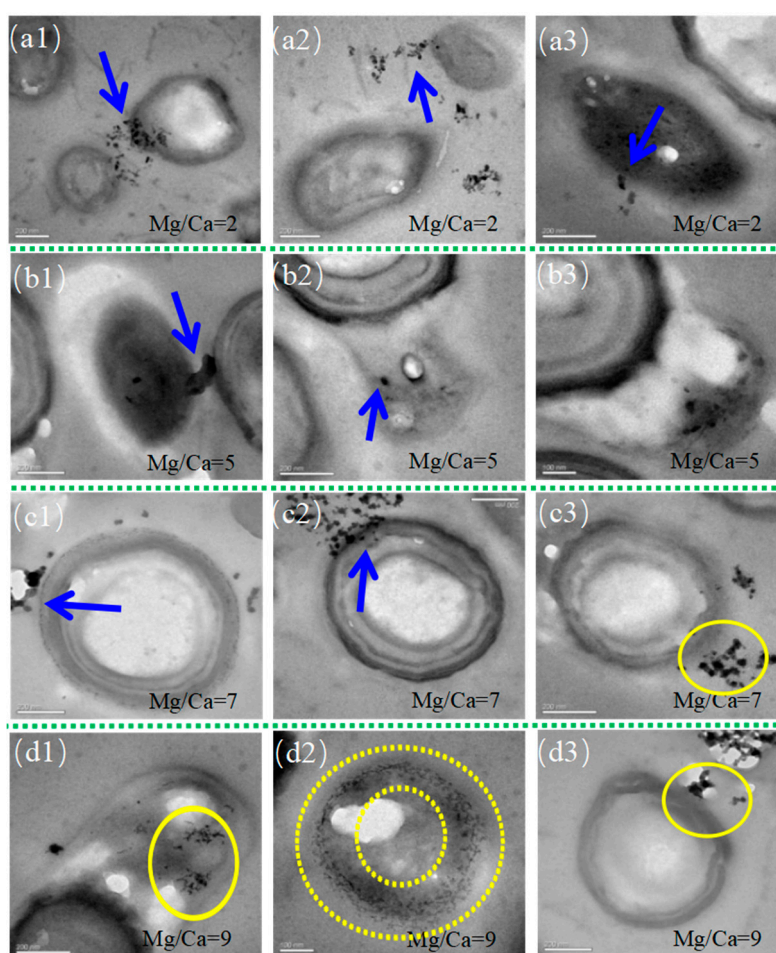


Figure 11. HRTEM analyses of biomineralization on the cell surface/EPS of *H. smyrnensis* WMS-3 bacteria at Mg/Ca molar ratios 2, 5, 7, and 9 (a1–3, b1–3, c1–3, and d1–3), respectively. (The blue arrows and yellow circles represent the location of minerals).

The opinions on EPS acting as the nucleation sites for biominerals has been widely accepted by researchers. It has been reported that aragonite-like CaCO_3 can be nucleated within the EPS of cyanobacteria, not on the cell wall, and higher concentrations of N and P can result in higher amounts of precipitation in the EPS [85]. EPS may have played an important role in the process of bacterially-induced biomineralization [70,86–88]. Deng et al. [86] have used the sulfate-reducing

bacteria (SRB) and halophilic bacteria to induce the precipitation of dolomite and found that the abundant EPS-like materials may have served as the template for dolomite nucleation while the heat-killed bacteria without EPS materials did not precipitate dolomite. It can be concluded that the EPS of bacteria indeed played an important role in the process of bacterially-induced biomineralization.

Moreover, the activation energy for nucleation (ΔG_N) could be calculated by the following equation [89]:

$$\Delta G_N = \frac{16\pi(\Delta G_1)^3}{3(kT\log_e S)^2} \quad (10)$$

where ΔG_1 was the interfacial energy, k the Boltzmann constant, T the temperature, and S the supersaturation. On the one hand, microorganisms could reduce ΔG_1 by providing the nucleation sites from EPS. On the other hand, the alkaline CA could catalyze the production of a large number of CO_3^{2-} and HCO_3^- ions to increase the supersaturation surrounding the EPS of the bacterial cell (S). As mentioned above these could reduce the nucleation energy barrier (ΔG_N) of biominerals and facilitate the nucleation on EPS.

In fact, the precipitation of biominerals induced by bacteria involves the controlled nucleation process at interfaces between the template macromolecules and minerals, e.g., the inorganic-organic molecular recognition processes [90]. However, the molecular interactions at the interface between the mineral and organic matrix are not well understood. Thus, the nucleation mechanism on EPS needs to be further explored. In this study, 15 kinds of amino acid were detected in the EPS of WMS-3 bacteria (Figure 12), among which glycine (Gly, 26.42%), alanine (Ala, 19.3%), glutamic acid (Glu, 17.76%) and aspartic acid (Asp, 10.05%) were the four amino acids with higher content (molar ratio). The pH value could increase to 8.9 under the influence of WMS-3 bacteria, which created an alkaline condition to facilitate the occurrence of amino acid deprotonation that could make the adsorbing of Ca^{2+} and Mg^{2+} ions to the EPS become much easier. Is that so? The elemental mapping (Figure S3) of *H. smyrnensis* WMS-3 proved that there was a large number of Ca^{2+} (Figure S3(a4,b3,c3)) and Mg^{2+} ions (Figure S3(b2,c2)) present inside the EPS, further illustrating the important role played by these amino acids in the EPS. Of course, some other organic substances could also be present within the EPS besides amino acids, and other organic substances affecting the nucleation should be studied in the future.

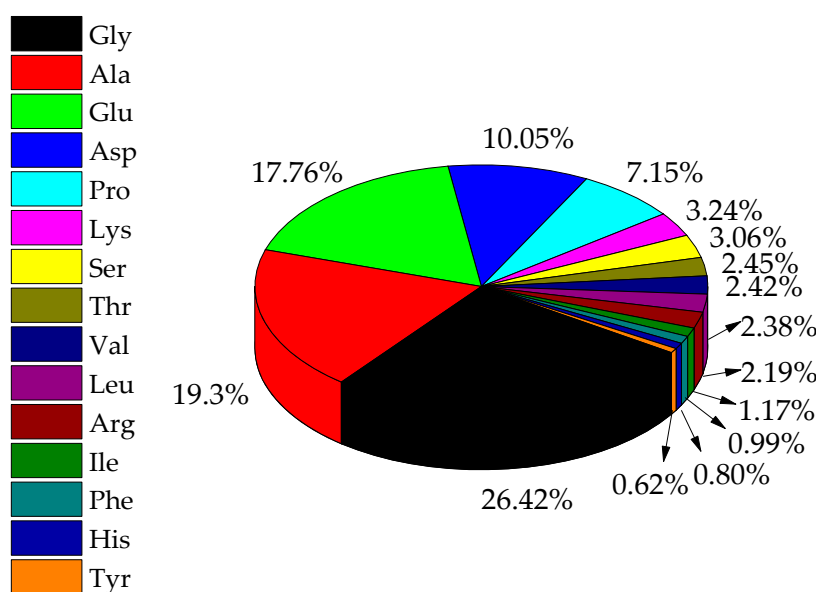


Figure 12. Amino acid composition (molar ratio) of the EPS from *H. smyrnensis* WMS-3.

3.7. Changes in the Intracellular Ca^{2+} Concentration

The dark nanometer-scale inclusions within the WMS-3 bacteria (Figure 10) demonstrates the occurrence of the intracellular biomineralization; moreover, the results of elemental mapping (Figure S3) reveal the presence of Ca^{2+} and Mg^{2+} ions inside the WMS-3 bacterial cells. The concentration of Ca^{2+} and Mg^{2+} ions is much higher than that inside the cell; thus, a concentration gradient was formed from the outside to the inside of the cell. Ca^{2+} and Mg^{2+} ions could enter the cell by diffusion along the ion channel. The changes of Ca^{2+} and Mg^{2+} ion concentration inside the bacterial cells need to be studied. Therefore, the fluorescence intensities of Ca^{2+} ions inside the WMS-3 bacterial cells marked with the Fluo-3 AM fluorescence indicator were determined, and the results are shown in Figure S4. It can be concluded that the fluorescence intensity of intracellular Ca^{2+} ion decreases with increasing Mg/Ca ratios, consistent with the results of Zhao et al. [91]. That is to say, Mg^{2+} ion concentration in the culture medium could strongly influence the diffusion of Ca^{2+} ions, resulting in a significant decrease in the concentration of intracellular Ca^{2+} ions ($p < 0.01$). The reason may be that Mg^{2+} ions with a smaller radius are able to go through the ion channels more easily than Ca^{2+} ions. The cell volume would remain unchanged, so that the more Mg^{2+} ions entered the cell, the less space there would be left for Ca^{2+} ions. In view of the lack of a fluorescence indicator for the Mg^{2+} ion, the intracellular Mg^{2+} ion concentration will be studied in the future.

4. Conclusions

The *H. smyrnensis* WMS-3 strain was identified by 16S rDNA homology comparison and this was used to induce the precipitation of calcium carbonate in a fluid containing 3% NaCl at different Mg/Ca ratios 0, 2, 5, 7, and 9. The results show that WMS-3 bacteria can increase the pH to about 9.0, due to the released ammonia and effects of CA; moreover, a large number of HCO_3^- and CO_3^{2-} ions produced by CA catalysis further elevated the supersaturation in the fluid. Higher pH and supersaturation promoted the biomineralization of calcium carbonate (calcite, Mg-rich calcite, aragonite, and monohydrocalcite) and only a little magnesium carbonate (hydromagnesite). The thermal stability of monohydrocalcite increased when an Mg/Ca ratio of 7 changes to 9, due to the crystallinity of monohydrocalcite at an Mg/Ca ratio of 9 being higher than that at an Mg/Ca ratio of 7. The abundant organic functional groups, a range of mineral shapes, negative stable carbon isotope values, and characteristics of surface chemistry proves the biogenesis of the minerals. Ca^{2+} ions entered the cell by diffusion to take part in the intracellular biomineralization. EPS could act as the nucleation sites for the precipitation of monohydrocalcite. This study sheds light on the biomineralization mechanism, facilitates the understanding of the formation process of monohydrocalcite in nature, and should be useful in interpreting the sedimentary record.

Supplementary Materials: The following are available online at <http://www.mdpi.com/2075-163X/9/10/632/s1>. Table S1: FWHM ($^\circ$) of monohydrocalcite induced by *H. smyrnensis* WMS-3 bacteria at Mg/Ca ratios of 7 and 9. Table S2: Stable carbon isotope $\delta^{13}\text{C}_{\text{PDB}}$ (‰) values of the biominerals. Figure S1: Rietveld refinement of XRD data (a, b, c, d and e represent Mg/Ca molar ratios of 0, 2, 5, 7 and 9, respectively). Figure S2: STEM and elemental mapping of *H. smyrnensis* WMS-3. (a: HRTEM analysis of minerals marked by the yellow circle in Figure 11c3 image; b: SAED analysis of minerals marked by the yellow circle in Figure 11d3 image) Figure S3: Fluorescence intensity of intracellular Ca^{2+} ions of *H. smyrnensis* WMS-3. (a, b and c represent Mg/Ca molar ratios of 0, 2 and 7, respectively). Figure S4: Fluorescence intensity of intracellular Ca^{2+} ions of *H. smyrnensis* WMS-3.

Author Contributions: Z.H. conceived and designed the experiments; J.P., Y.Z. and Y.W. performed the experiments; Z.H., H.Z., and H.Y. analyzed the results of all the experiments; J.P. and H.Y. wrote the paper; H.Z. and M.E.T. revised the manuscript; J.Z. helped us to analyze the data by using SPSS 21 software; M.J. helped us to modify figures, Y.Z. helped us to do some experiments, Rietveld refinement was performed by Y.Z., and the calculation of SI by using PHREEQC software in response letter was performed by B.S. All authors have read and approved the manuscript.

Funding: This work was supported by the National Natural Science Foundation of China (41772095, 41972108, U1663201, 41702131); the Laboratory for Marine Mineral Resources, Qingdao National Laboratory for Marine Science and Technology (MMRZZ201804); Taishan Scholar Talent Team Support Plan for Advanced & Unique Discipline Areas, Major Scientific and Technological Innovation Projects of Shandong Province (2017CXGC1602,

2017CXGC1603); SDUST Research Fund (2015TDJH101); Natural Science Foundation of Shandong Province (ZR2019MD027, ZR2017BD001); the Scientific and Technological Innovation Project Financially Supported by Qingdao National Laboratory for Marine Science and Technology (2016ASKJ13); National College Students' Innovation and Entrepreneurship Training Program (201910424017).

Conflicts of Interest: The authors declare no conflict of interest.

References

1. Lv, D.; Li, Z.; Chen, J.; Liu, H.; Guo, J.; Shang, L. Characteristics of the Permian coal-formed gas sandstone reservoirs in Bohai Bay Basin and the adjacent areas, North China. *J. Pet. Sci. Eng.* **2011**, *78*, 516–528. [[CrossRef](#)]
2. Yu, H.; Yuan, J.; Guo, W.; Cheng, J.; Hu, Q. A preliminary laboratory experiment on coalbed methane displacement with carbon dioxide injection. *Int. J. Coal. Geol.* **2008**, *73*, 156–166. [[CrossRef](#)]
3. Yu, H.; Zhou, G.; Fan, W.; Ye, J. Predicted CO₂ enhanced coalbed methane recovery and CO₂ sequestration in China. *Int. J. Coal Geol.* **2007**, *71*, 345–357. [[CrossRef](#)]
4. Yu, H.; Zhou, L.; Guo, W.; Cheng, J.; Hu, Q. Predictions of the adsorption equilibrium of methane/carbon dioxide binary gas on coals using Langmuir and ideal adsorbed solution theory under feed gas conditions. *Int. J. Coal Geol.* **2008**, *73*, 115–129. [[CrossRef](#)]
5. Pang, Y.; Guo, X.; Han, Z.; Zhang, X.; Zhu, X.; Hou, F.; Han, C.; Song, Z.; Xiao, G. Mesozoic–Cenozoic denudation and thermal history in the Central Uplift of the South Yellow Sea basin and the implications for hydrocarbon systems: Constraints from the CSDP-2 borehole. *Mar. Petrol. Geol.* **2019**, *99*, 355–369. [[CrossRef](#)]
6. Allwood, A.C.; Walter, M.R.; Kamber, B.S.; Marshall, C.P.; Burch, I.W. Stromatolite reef from the Early Archaean era of Australia. *Nature* **2006**, *441*, 714–718. [[CrossRef](#)] [[PubMed](#)]
7. Allwood, A.C.; Walter, M.R.; Burch, I.W.; Kamber, B.S. 3.43 billion-year-old stromatolite reef from the Pilbara Craton of western Australia: Ecosystem-scale insights to early life on Earth. *Precambrian Res.* **2007**, *158*, 198–227. [[CrossRef](#)]
8. Lindsay, J.F.; Brasier, M.D.; Mcloughlin, N.; Green, O.R.; Fogel, M.; Mcnamara, K.M.; Steele, A.; Mertzman, S.A. Abiotic earth-establishing a baseline for earliest life, data from the Archean of western Australia. In Proceedings of the Lunar & Planetary Science Conference, League, TX, USA, 17–21 March 2003.
9. Dupraz, C.; Reid, R.P.; Braissant, O.; Decho, A.W.; Norman, R.S.; Visscher, P.T. Processes of carbonate precipitation in modern microbial mats. *Earth-Sci. Rev.* **2009**, *96*, 141–162. [[CrossRef](#)]
10. Chough, S.K.; Lee, H.S.; Woo, J.; Chen, J.; Choi, D.K.; Lee, S.-b.; Kang, I.; Park, T.-y.; Han, Z. Cambrian stratigraphy of the North China Platform: Revisiting principal sections in Shandong Province, China. *Geosci. J.* **2010**, *14*, 235–268. [[CrossRef](#)]
11. Lee, J.-H.; Chen, J.; Chough, S.K. Paleoenvironmental implications of an extensive maceriate microbialite bed in the Furongian Chaomidian Formation, Shandong Province, China. *Palaeogeogr. Palaeoclimatol. Palaeoecol.* **2010**, *297*, 621–632. [[CrossRef](#)]
12. Lv, D.; Chen, J. Depositional environments and sequence stratigraphy of the Late Carboniferous–Early Permian coal-bearing successions (Shandong Province, China): Sequence development in an epicontinental basin. *J. Asian Earth Sci.* **2014**, *79*, 16–30. [[CrossRef](#)]
13. Yin, S.; Lv, D.; Jin, L.; Ding, W. Experimental analysis and application of the effect of stress on continental shale reservoir brittleness. *J. Geophys. Eng.* **2018**, *15*, 478–494. [[CrossRef](#)]
14. Xu, Y.; Shen, X.; Chen, N.; Yang, C.; Wang, Q. Evaluation of reservoir connectivity using whole-oil gas chromatographic fingerprint technology: A case study from the Es₃³ reservoir in the Nanpu Sag, China. *Pet. Sci. Technol.* **2012**, *9*, 290–294. [[CrossRef](#)]
15. Chen, J.; Van Loon, A.J.; Han, Z.; Chough, S.K. Funnel-shaped, breccia-filled clastic dykes in the Late Cambrian Chaomidian Formation (Shandong Province, China). *Sediment. Geol.* **2009**, *221*, 1–6. [[CrossRef](#)]
16. Chen, J.; Chough, S.K.; Chun, S.S.; Han, Z. Limestone pseudoconglomerates in the Late Cambrian Gushan and Chaomidian Formations (Shandong Province, China): Soft-sediment deformation induced by storm-wave loading. *Sedimentology* **2010**, *56*, 1174–1195. [[CrossRef](#)]
17. Chen, J.; Han, Z.; Zhang, X.; Fan, A.; Yang, R. Early diagenetic deformation structures of the Furongian ribbon rocks in Shandong Province of China—A new perspective of the genesis of limestone conglomerates. *Sci. China Earth Sci.* **2010**, *53*, 241–252. [[CrossRef](#)]

18. Chen, J.; Chough, S.K.; Han, Z.; Lee, J.-H. An extensive erosion surface of a strongly deformed limestone bed in the Gushan and Chaomidian formations (late Middle Cambrian to Furongian), Shandong Province, China: Sequence-stratigraphic implications. *Sediment. Geol.* **2011**, *233*, 129–149. [[CrossRef](#)]
19. Chen, J.; Chough, S.K.; Lee, J.-H.; Han, Z. Sequence-stratigraphic comparison of the upper Cambrian Series 3 to Furongian succession between the Shandong region, China and the Taebaek area, Korea: High variability of bounding surfaces in an epeiric platform. *Geosci. J.* **2012**, *16*, 357–379. [[CrossRef](#)]
20. Lee, J.; Chen, J.; Choh, S.; Lee, D.; Han, Z.; Chough, S.K. Furongian (Late Cambrian) sponge–microbial maze-like reefs in the north china platform. *Palaios* **2014**, *29*, 27–37. [[CrossRef](#)]
21. Van Loon, A.J.T.; Han, Z.; Han, Y. Origin of the vertically orientated clasts in brecciated shallow-marine limestones of the Chaomidian Formation (Furongian, Shandong Province, China). *Sedimentology* **2013**, *60*, 1059–1070. [[CrossRef](#)]
22. Woo, J.; Chough, S.K.; Han, Z. Chambers of *Epiphyton thalli* in microbial buildups, Zhangxia Formation (Middle Cambrian), Shandong Province, China. *Palaios* **2008**, *23*, 55–64. [[CrossRef](#)]
23. Park, T.Y.; Sang, J.M.; Han, Z.; Choi, D.K. Ontogeny of the middle cambrian trilobite shantungia spinifera walcott, 1905 from north china and its taxonomic significance. *J. Paleontol.* **2008**, *82*, 851–855. [[CrossRef](#)]
24. Liu, Y.; Jiao, X.; Li, H.; Yuan, M.; Yang, W.; Zhou, X.; Liang, H.; Zhou, D.; Zheng, C.; Sun, Q.; et al. Primary dolostone formation related to mantle-originated exhalative hydrothermal activities, Permian Yuejingou section, Santanghu area, Xinjiang, NW China. *Sci. China Earth Sci.* **2012**, *55*, 183–192. [[CrossRef](#)]
25. Han, Z.; Zhang, X.; Chi, N.; Han, M.; Woo, J.; Lee, H.S.; Chen, J. Cambrian oncoids and other microbial-related grains on the North China Platform. *Carbonates Evaporites* **2015**, *30*, 373–386. [[CrossRef](#)]
26. Fan, A.; Yang, R.; van Loon, A.J.; Yin, W.; Han, Z.; Zavala, C. Classification of gravity-flow deposits and their significance for unconventional petroleum exploration, with a case study from the Triassic Yanchang Formation (southern Ordos Basin, China). *J. Asian Earth Sci.* **2018**, *161*, 57–73. [[CrossRef](#)]
27. Chang, X.; Wang, T.G.; Li, Q.; Cheng, B.; Tao, X. Geochemistry and possible origin of petroleum in Palaeozoic reservoirs from Halahatang Depression. *J. Asian Earth Sci.* **2013**, *74*, 129–141. [[CrossRef](#)]
28. Dahl, K.; Buchardt, B. Monohydrocalcite in the Arctic Ikka Fjord, SW Greenland: First reported marine occurrence. *J. Sediment. Res.* **2006**, *76*, 460–471. [[CrossRef](#)]
29. Rivadeneyra, M.A.; Delgado, G.; Ramos-Cormenzana, A.; Delgado, R. Biomineralization of carbonates by *Halomonas eurihalina* in solid and liquid media with different salinities: Crystal formation sequence. *Res. Microbiol.* **1998**, *149*, 277–287. [[CrossRef](#)]
30. Rivadeneyra, M.A.; Delgado, G.; Ramos-Cormenzana, A.; Delgado, R. Precipitation of carbonates by *Deleya halophila* in liquid media: Pedological implications in saline soils. *Arid Soil Res. Rehab.* **1997**, *11*, 35–47. [[CrossRef](#)]
31. Rivadeneyra, M.A.; Delgado, R.; Delgado, G.; Moral, A.D.; Ferrer, M.R.; Ramos-Cormenzana, A. Precipitation of carbonates by *Bacillus sp.* isolated from saline soils. *Geomicrobiol. J.* **1993**, *11*, 175–184. [[CrossRef](#)]
32. Rivadeneyra, M.A.; Párraga, J.; Delgado, R.; Ramos-Cormenzana, A.; Delgado, G. Biomineralization of carbonates by *Halobacillus trueperi* in solid and liquid media with different salinities. *FEMS Microbiol. Ecol.* **2004**, *48*, 39–46. [[CrossRef](#)] [[PubMed](#)]
33. Arias, D.; Cisternas, L.A.; Rivas, M. Biomineralization of calcium and magnesium crystals from seawater by *halotolerant* bacteria isolated from Atacama Salar (Chile)(Article). *Desalination* **2017**, *405*, 1–9. [[CrossRef](#)]
34. Han, Z.; Li, D.; Zhao, H.; Yan, H.; Li, P. Precipitation of carbonate minerals induced by the halophilic *Chromohalobacter israelensis* under high salt concentrations: Implications for natural environments. *Minerals* **2017**, *7*, 95. [[CrossRef](#)]
35. Rivadeneyra, M.A.; Martín-Algarra, A.; Sánchez-Navas, A.; Martín-Ramos, D. Carbonate and phosphate precipitation by *Chromohalobacter marismortui*. *Geomicrobiol. J.* **2006**, *23*, 89–101. [[CrossRef](#)]
36. Han, Z.; Wang, J.; Zhao, H.; Tucker, M.E.; Zhao, Y.; Wu, G.; Zhou, J.; Yin, J.; Zhang, H.; Zhang, X.; et al. Mechanism of biomineralization induced by *Bacillus subtilis* J2 and characteristics of the biominerals. *Minerals* **2019**, *9*, 218. [[CrossRef](#)]
37. Zhuang, D.; Yan, H.; Tucker, M.E.; Zhao, H.; Han, Z.; Zhao, Y.; Sun, B.; Li, D.; Pan, J.; Zhao, Y.; et al. Calcite precipitation induced by *Bacillus cereus* MRR2 cultured at different Ca²⁺ concentrations: Further insights into biotic and abiotic calcite. *Chem. Geol.* **2018**, *500*, 64–87. [[CrossRef](#)]

38. Han, Z.; Meng, R.; Yan, H.; Zhao, H.; Han, M.; Zhao, Y.; Sun, B.; Sun, Y.; Wang, J.; Zhuang, D. Calcium carbonate precipitation by *Synechocystis* sp. PCC6803 at different Mg/Ca molar ratios under the laboratory condition. *Carbonates Evaporites* **2017**. [[CrossRef](#)]
39. Han, Z.; Yan, H.; Zhao, H.; Zhou, S.; Han, M.; Meng, X.; Zhang, Y.; Zhao, Y.; Sun, B.; Yao, C.; et al. Bio-precipitation of calcite with preferential orientation induced by *Synechocystis* sp. PCC6803. *Geomicrobiol. J.* **2014**, *31*, 884–899. [[CrossRef](#)]
40. Arvidson, R.S.; Mackenzie, F.T. The dolomite problem: Control of precipitation kinetics by temperature and saturation state. *Am. J. Sci.* **1999**, *299*, 257–288. [[CrossRef](#)]
41. Liu, F.; Csetenyi, L.; Gadd, G.M. Amino acid secretion influences the size and composition of copper carbonate nanoparticles synthesized by ureolytic fungi. *Appl. Microbiol. Biot.* **2019**, *103*, 7217–7230. [[CrossRef](#)]
42. Morgan, J.W.; Forster, C.F.; Evison, L. A comparative study of the nature of biopolymers extracted from anaerobic and activated sludges. *Water. Res.* **1990**, *24*, 743–750. [[CrossRef](#)]
43. Su, T.; Shao, Q.; Qin, Z.; Guo, Z.; Wu, Z. Role of interfaces in two-dimensional photocatalyst for water splitting. *Acs. Catal.* **2018**, *8*, 2253–2276. [[CrossRef](#)]
44. Ding, Y.; Yang, B.; Hao, L.; Liu, Z.; Xiao, Z.; Zheng, X.; Liu, Q. FePt-Au ternary metallic nanoparticles with the enhanced peroxidase-like activity for ultrafast colorimetric detection of H₂O₂. *Sensor Actuat. B-chem* **2017**, *259*, 775–783. [[CrossRef](#)]
45. Zhang, X.; Wu, Y.; Sun, Y.; Ding, P.; Liu, Q.; Lin, T.; Guo, J. Hybrid of Fe₄[Fe(CN)₆]₃ nanocubes and MoS₂ nanosheets on nitrogen-doped graphene realizing improved electrochemical hydrogen production. *Electrochim. Acta.* **2018**, *263*, 140–146. [[CrossRef](#)]
46. Wei, C.; Liu, Q.; Zhu, X.; Min, F. One-step in situ growth of magnesium ferrite nanorods on graphene and their microwave-absorbing properties. *Appl. Organomet. Chem.* **2018**, *32*, 4011–4019. [[CrossRef](#)]
47. Zhang, X.; Sun, Y.; Liu, Q.; Guo, J.; Xiao, Z. FePt nanoalloys on N-doped graphene paper as integrated electrode towards efficient formic acid electrooxidation. *J. Appl. Electrochem.* **2018**, *48*, 95–103. [[CrossRef](#)]
48. Lin, C.; Hu, L.; Cheng, C.; Sun, K.; Guo, X.; Shao, Q.; Li, J.; Wang, N.; Guo, Z. Nano-TiNb₂O₇/carbon nanotubes composite anode for enhanced lithium-ion storage. *Electrochim. Acta* **2018**, *260*, 65–72. [[CrossRef](#)]
49. Pan, D.; Ge, S.; Zhang, X.; Mai, X.; Li, S.; Guo, Z. Synthesis and photoelectrocatalytic activity of In₂O₃ hollow microspheres via a bio-template route using yeast templates. *Dalton Trans.* **2018**, *47*, 708–715. [[CrossRef](#)]
50. Han, Z.; Gao, X.; Zhao, H.; Tucker, M.E.; Zhao, Y.; Bi, Z.; Pan, J.; Wu, G.; Yan, H. Extracellular and intracellular biomineralization induced by *Bacillus Licheniformis* DB1-9 at different Mg/Ca molar ratios. *Minerals* **2018**, *8*, 585. [[CrossRef](#)]
51. Han, Z.; Sun, B.; Zhao, H.; Yan, H.; Han, M.; Zhao, Y.; Meng, R.; Zhuang, D.; Li, D.; Ma, Y.; et al. Isolation of *Leclercia adcarboxglata* strain JLS1 from dolostone sample and characterization of its induced struvite. *Geomicrobiol. J.* **2017**, *34*, 500–510. [[CrossRef](#)]
52. Han, Z.; Yu, W.; Zhao, H.; Zhao, Y.; Tucker, M.E.; Yan, H. The significant roles of Mg/Ca ratio, Cl⁻ and SO₄²⁻ in carbonate mineral precipitation by the Halophile *Staphylococcus epidermis* Y2. *Minerals* **2018**, *8*, 594. [[CrossRef](#)]
53. Power, I.M.; Harrison, A.L.; Dipple, G.M. Accelerating mineral carbonation using carbonic anhydrase. *Environ. Sci. Technol.* **2016**, *50*, 2610–2618. [[CrossRef](#)]
54. Lee, S.W.; Park, S.B.; Jeong, S.K.; Lim, K.S.; Lee, S.H.; Trachtenberg, M.C. On carbon dioxide storage based on biomineralization strategies. *Micron* **2010**, *41*, 273–282. [[CrossRef](#)] [[PubMed](#)]
55. Power, I.M.; Harrison, A.L.; Dipple, G.M.; Southam, G. Carbon sequestration via carbonic anhydrase facilitated magnesium carbonate precipitation. *Int. J. Greenh. Gas Control* **2013**, *16*, 145–155. [[CrossRef](#)]
56. Qiu, X.; Wang, H.; Yao, Y.; Duan, Y. High salinity facilitates dolomite precipitation mediated by *Haloferax volcanii* DS52. *Earth. Planet. Sci. Lett.* **2017**, *472*, 197–205. [[CrossRef](#)]
57. Katz, A.K.; Glusker, J.P.; Beebe, S.A.; Bock, C.W. Calcium ion coordination: A comparison with that of beryllium, magnesium, and zinc. *J. Am. Chem. Soc.* **1996**, *118*, 5752–5763. [[CrossRef](#)]
58. Xu, J.; Yan, C.; Zhang, F.; Konishi, H.; Xu, H.; Teng, H.H. Testing the cation-hydration effect on the crystallization of Ca-Mg-CO₃ systems. *Proc. Natl. Acad. Sci. USA* **2013**, *110*, 17750–17755. [[CrossRef](#)]
59. Rodriguez-Blanco, J.D.; Shaw, S.; Bots, P.; Roncal-Herrero, T.; Benning, L.G. The role of Mg in the crystallization of monohydrocalcite. *Geochim. Cosmochim. Acta* **2014**, *127*, 204–220. [[CrossRef](#)]
60. Stoffers, P.; Fischbeck, R. Monohydrocalcite in the sediments of Lake Kivu (East Africa). *Sedimentology* **2010**, *21*, 163–170. [[CrossRef](#)]

61. Hull, H.; Turnbull, A.G. A thermochemical study of monohydrocalcite. *Geochim. Cosmochim. Acta* **1973**. [[CrossRef](#)]
62. Munemoto, T.; Fukushi, K. Transformation kinetics of monohydrocalcite to aragonite in aqueous solutions. *J. Miner. Petrol. Sci.* **2008**, *103*, 345–349. [[CrossRef](#)]
63. Kalmar, L.; Homola, D.; Varga, G.; Tompa, P. Structural disorder in proteins brings order to crystal growth in biomineralization. *Bone* **2012**, *51*, 528–534. [[CrossRef](#)] [[PubMed](#)]
64. Jönsson, M.; Persson, D.; Thierry, D. Corrosion product formation during NaCl induced atmospheric corrosion of magnesium alloy AZ91D. *Corros. Sci.* **2007**, *49*, 1540–1558. [[CrossRef](#)]
65. Bizani, D.; Motta, A.S.; Morrissy, J.A.; Terra, R.M.; Souto, A.A.; Brandelli, A. Antibacterial activity of cerein 8A, a bacteriocin-like peptide produced by *Bacillus cereus*. *Int. Microbiol.* **2005**, *8*, 125–131. [[CrossRef](#)]
66. Wang, Y.; Yao, Q.; Zhou, G.; Fu, S. Formation of elongated calcite mesocrystals and implication for biomineralization. *Chem. Geol.* **2013**, *360*, 126–133. [[CrossRef](#)]
67. Zhou, G.; Guan, Y.; Yao, Q.; Fu, S. Biomimetic mineralization of prismatic calcite mesocrystals: Relevance to biomineralization. *Chem. Geol.* **2010**, *279*, 63–72. [[CrossRef](#)]
68. Zhang, C.; Lv, J.; Li, F.; Li, X. Nucleation and growth of mg-calcite spherulites induced by the bacterium *Curvibacter Lanceolatus* strain HJ-1. *Microsc. Microanal.* **2017**, *23*, 1–8. [[CrossRef](#)]
69. Buczynski, C.; Chafetz, H. Habit of bacterially induced precipitates of calcium carbonate and the influences of medium viscosity on mineralogy. *J. Sediment. Res.* **1991**, *61*, 226–233. [[CrossRef](#)]
70. Sánchez-Román, M.; McKenzie, J.A.; Wagener, A.D.L.R.; Rivadeneyra, M.A.; Vasconcelos, C. Presence of sulfate does not inhibit low-temperature dolomite precipitation. *Earth. Planet. Sci. Lett.* **2009**, *285*, 131–139. [[CrossRef](#)]
71. Sánchez-Román, M.; Romanek, C.S.; Fernández-Remolar, D.C.; Sánchez-Navas, A.; McKenzie, J.A.; Pibernat, R.A.; Vasconcelos, C. Aerobic biomineralization of Mg-rich carbonates: Implications for natural environments. *Chem. Geol.* **2011**, *281*, 143–150. [[CrossRef](#)]
72. Jones, M.; Donnelly, A. Carbon sequestration in temperate grassland ecosystems and the influence of management, climate and elevated CO₂: Tansley review. *New Phytol.* **2004**, *164*, 423–439. [[CrossRef](#)]
73. Haurie, L.; Fernandez, A.I.; Velasco, J.I.; Chimenos, J.M.; Lopez-Cuesta, J.M.; Espiell, F. Effects of milling on the thermal stability of synthetic hydromagnesite. *Mater. Res. Bull.* **2007**, *42*, 1010–1018. [[CrossRef](#)]
74. Kimura, T.; Koga, N. Monohydrocalcite in comparison with hydrated amorphous calcium carbonate: Precipitation condition and thermal behavior. *Crysl. Growth Des.* **2011**, *11*, 3877–3884. [[CrossRef](#)]
75. Ma, K.; Cui, L.; Dong, Y.; Wang, T.; Da, C.; Hirasaki, G.J.; Biswal, S.L. Adsorption of cationic and anionic surfactants on natural and synthetic carbonate materials. *J. Colloid Interf. Sci* **2013**, *408*, 164–172. [[CrossRef](#)] [[PubMed](#)]
76. Ardizzone, S.; Bianchi, C.L.; Fadoni, M.; Vercelli, B. Magnesium salts and oxide: An XPS overview. *Appl. Surf. Sci.* **1997**, *119*, 253–259. [[CrossRef](#)]
77. Paulo, C.; Kenney, J.P.L.; Persson, P.; Dittrich, M. Effects of phosphorus in growth media on biomineralization and cell surface properties of marine cyanobacteria synechococcus. *Geosciences* **2018**, *8*, 471. [[CrossRef](#)]
78. Huang, Y.; Yao, Q.; Li, H.; Wang, F.; Zhou, G.; Fu, S. Aerobically incubated bacterial biomass-promoted formation of disordered dolomite and implication for dolomite formation. *Chem. Geol.* **2019**, *523*, 19–30. [[CrossRef](#)]
79. Hsu, M.; Chuang, H.; Cheng, F.; Huang, Y.; Han, C.; Pao, K.; Chou, S.; Shieh, F.K.; Tsai, F.Y.; Lin, C.; et al. Simple and highly efficient direct thiolation of the surface of carbon nanotubes. *RSC Adv.* **2014**, *4*, 14777–14780. [[CrossRef](#)]
80. Fein, J.B.; Martin, A.M.; Wightman, P.G. Metal adsorption onto bacterial surfaces: Development of a predictive approach. *Geochim. Cosmochim. Acta* **2001**, *65*, 4267–4273. [[CrossRef](#)]
81. Couradeau, E.; Benzerara, K.; Gérard, E.; Moreira, D.; Bernard, S.; Brown, G.; Lopez-Garcia, P. An early-branching microbialite cyanobacterium forms intracellular carbonates. *Science* **2012**, *336*, 459–462. [[CrossRef](#)]
82. Benzerara, K.; Skouri-Panet, F.; Li, J.; Ferard, C.; Gugger, M.; Laurent, T.; Couradeau, E.; Ragon, M.; Cosmidis, J.; Menguy, N.; et al. Intracellular Ca-carbonate biomineralization is widespread in cyanobacteria. *Proc. Natl. Acad. Sci. USA* **2014**, *111*, 10933. [[CrossRef](#)] [[PubMed](#)]
83. Keim, C.; Solórzano, I.; Farina, M.; Lins, U. Intracellular inclusions of uncultured magnetotactic bacteria. *Int. Microbiol.* **2005**, *8*, 111–117. [[CrossRef](#)]

84. Perri, E.; Tucker, M.; Slowakiewicz, M.; Whitaker, F.; Bowen, L.; Perrotta, I. Carbonate and silicate biomineralization in a hypersaline microbial mat (Mesaieed sabkha, Qatar): Roles of bacteria, extracellular polymeric substances and viruses. *Sedimentology* **2017**, *65*, 1213–1245. [[CrossRef](#)]
85. Obst, M.; Dynes, J.J.; Lawrence, J.R.; Swerhone, G.D.W.; Benzerara, K.; Karunakaran, C.; Kaznatcheev, K.; Tyliczszak, T.; Hitchcock, A.P. Precipitation of amorphous CaCO₃ (aragonite-like) by cyanobacteria: A STXM study of the influence of EPS on the nucleation process. *Geochim. Cosmochim. Acta* **2009**, *73*, 4180–4198. [[CrossRef](#)]
86. Deng, S.; Dong, H.; Lv, G.; Jiang, H.; Yu, B.; Bishop, M.E. Microbial dolomite precipitation using sulfate reducing and halophilic bacteria: Results from Qinghai Lake, Tibetan Plateau, NW China. *Chem. Geol.* **2010**, *278*, 151–159. [[CrossRef](#)]
87. Kenward, P.A.; Goldstein, R.H.; Gonzalez, L.A.; Roberts, J.A. Precipitation of low-temperature dolomite from an anaerobic microbial consortium: The role of methanogenic Archaea. *Geobiology* **2009**, *7*, 556–565. [[CrossRef](#)]
88. Bontognali, T.R.R.; Vasconcelos, C.; Warthmann, R.J.; Bernasconi, S.M.; Dupraz, C.; Strohmenger, C.J.; Mckenzie, J.A. Dolomite formation within microbial mats in the coastal sabkha of Abu Dhabi (United Arab Emirates). *Sedimentology* **2010**, *57*, 824–844. [[CrossRef](#)]
89. Lv, J.; Ma, F.; Li, F.; Zhang, C.; Chen, J. Vaterite induced by *Lysinibacillus* sp. GW-2 strain and its stability. *J. Struct. Biol.* **2017**, *200*, 97–105. [[CrossRef](#)]
90. Mann, S.; Heywood, B.R.; Rajam, S.; Wade, V.J. Molecular recognition in biomineralization. In *Mechanisms and Phylogeny of Mineralization in Biological Systems*; Suga, S., Nakahara, H., Eds.; Springer: Tokyo, Japan, 1991; pp. 47–55.
91. Zhao, Y.; Yan, H.; Zhou, J.; Tucker, M.E.; Han, M.; Zhao, H.; Mao, G.; Zhao, Y.; Han, Z. Bio-precipitation of calcium and magnesium ions through extracellular and intracellular process induced by *Bacillus Licheniformis* SRB2. *Minerals* **2019**, *9*, 526. [[CrossRef](#)]



© 2019 by the authors. Licensee MDPI, Basel, Switzerland. This article is an open access article distributed under the terms and conditions of the Creative Commons Attribution (CC BY) license (<http://creativecommons.org/licenses/by/4.0/>).